Impact dynamics of nanodroplets on pillared surfaces

Yi-Feng Wang,[1,2] Yi-Bo Wang,[1,2] Ling-Zhe Zhang,[1,2] Xin He,[1,2] Yan-Ru Yang,[1,2] Xiao-Dong Wang,[1,2,*] and Duu-Jong Lee[3,4,†]

[1]*State Key Laboratory of Alternate Electrical Power System with Renewable Energy Sources, North China Electric Power University, Beijing 102206, China*

[2]*Research Center of Engineering Thermophysics, North China Electric Power University, Beijing 102206, China*

[3]*Department of Mechanical Engineering, City University of Hong Kong, Kowloon Tong 999077, Hong Kong*

[4]*Department of Chemical Engineering & Materials Science, Yuan Ze University, Chung-Li 32003, Taiwan*

(Received 4 March 2024; accepted 28 June 2024; published 23 July 2024)

This work investigates impacting nanodroplets on pillared surfaces via molecular dynamics (MD) simulations, especially to understand the intrusion effect of liquid in pillar gaps at the nanoscale, by comprehensively revealing outcome regimes and modeling the maximum spreading factor (β_{max}). A total of six outcomes, including first sticky (1S), second sticky (2S), first nonbouncing (1NB), second nonbouncing (2NB), first bouncing (1B), and second bouncing (2B), are identified. The 1S, 2S, and 2B regimes take place on monostable Wenzel surfaces with the Wenzel-to-Cassie dewetting transition and bouncing boundaries separating them; the 1NB, 2NB, 1B, and 2B regimes occur on monostable Cassie surfaces, distinguished by the Cassie-to-Wenzel wetting transition and bouncing boundaries. By establishing criteria of all boundaries, a universal phase diagram of impacting nanodroplets on pillared surfaces is constructed. Besides, to understand the altered spreading dynamics by the liquid intrusion effect, β_{max} is modeled. The bulk droplet above pillared surfaces is found to have the same spreading dynamics as a nanodroplet on flat surfaces, which decouples the effects of the bulk droplet and the liquid intruding into pillar gaps. Subsequently, two intrusion regimes are classified based on different intrusion morphology of the liquid front, and the scalings for intrusion volume in different intrusion regimes are obtained with the corresponding transition criterion being proposed. Eventually, scaling laws of β_{max} for impacting nanodroplets on pillared surfaces are established by incorporating the volume term of the bulk droplet, and are in good agreement with all available MD data of β_{max}, showing their strong robustness and universality.

DOI: 10.1103/PhysRevFluids.9.073602

I. INTRODUCTION

The phenomenon of a droplet impacting a surface is ubiquitous in natural life, for example, rain droplets impacting roofs, and in technical applications, such as inkjet printing [1], anti-icing surface design [2], spray spraying cooling [3], coating [4], and others. After impacting surfaces, many outcomes could take place by impacting droplets, such as deposition, splashing, breakup, and bouncing [5]. Identifying outcome regimes is a classical problem owing to its practical significance. For instance, deposition is welcome in inkjet printing, while bouncing is favored in anti-icing surface design. Besides identifying outcomes, modeling the maximum spreading factor, $\beta_{max}(=D_{max}/D_0)$,

*Contact author: wangxd99@gmail.com
†Contact author: tuclee@cityu.edu.hk

is also a classical problem since dominant forces and the mechanisms of viscous dissipation can be effectively understood by modeling it, where D_{max} is the maximum spreading diameter and D_0 is the initial diameter of impacting droplets. Many efforts have been devoted to studying the two classical problems through experiments [6–12], numerical simulations [13–15], and theoretical analyses [6,9–13,16,17].

As compared with the frequently studied millimeter-sized droplets, the impact dynamics of nanodroplets has recently aroused increasing interest, owing to their use in emerging and rising nanotechnologies like nanoscale inkjet printing [18], anti-icing surface design [19], synthesizing high-entropy materials [20], accelerating drug discovery [21], and so forth. Therefore, understanding the underlying mechanisms of impacting nanodroplets on surfaces is urgently desired. Within this context, substantial recent numerical and theoretical studies have been reported to investigate impacting nanodroplets in one decade. In the early research stage, the impact dynamics of nanodroplets is focused on flat surfaces with wettability ranging from hydrophilic to superhydrophobic and it is considered to be controlled by the parameter group of We, Oh (or Re), and θ [22–25], where the Weber number ($\mathrm{We} = \rho D_0 V_0^2/\gamma$) represents the ratio of inertial to capillary forces, the Ohnesorge number, $\mathrm{Oh} = \mu/(\rho D_0 \gamma)^{1/2}$, denotes the ratio of viscous to inertial-capillary forces, the Reynolds number ($\mathrm{Re} = \rho D_0 V_0/\mu$) stands for the ratio of inertial to viscous forces, and the intrinsic contact angle, θ, is the angle at the three-phase contact line for a sessile droplet equilibrating on a flat surface; ρ is the liquid density, V_0 is the impact velocity, γ is the surface tension, and μ is the liquid viscosity. With the help of molecular dynamics (MD) simulations which are effective for investigating such small droplets, certain studies have claimed that the impact dynamics of nanodroplets is distinct from millimeter-sized droplets due to various scale effects, where scale effects are the key reasons that the dynamics across scales are different [22,23,26,27]. To our best knowledge, three primary scale effects have been reported. First, when the droplet diameter decreases from the macroscale to the nanoscale, Oh has a thousandfold increase, indicating that the viscous force becomes important at the nanoscale [22]. Second, unlike viscous dissipation, which mainly takes place in the boundary layer near solid walls for macroscale droplets, violent velocity gradients have been found in entire impacting nanodroplets, showing the viscous dissipation mechanism has altered when decreasing the droplet diameter to the nanoscale [27]. Third, violating the no-slip condition accepted for impacts of macroscale droplets, significant slip has been found for impacting nanodroplets [28]. Because of the occurrence of scale effects, previous models for millimeter-sized droplets must not be valid for nanodroplets, and, thereby, many studies revisited the classical problems (identifying outcome regimes and modeling β_{max}) of impacting nanodroplets on flat surfaces [27,29–34]. For example, on modeling β_{max}, a low-viscosity millimeter-sized droplet impacting on a superhydrophobic surface is attested to be controlled by only inertial and capillary forces, i.e., in the capillary regime, and satisfies the We-dependent scaling law of $\beta_{max} \sim \mathrm{We}^{1/4}$ over a three-order-of-magnitude-wide range of Weber numbers [35]; however, Wang *et al.* [22] indicated that impacting nanodroplets in the capillary regime, controlled by inertial and capillary forces, do not follow the scaling law of $\beta_{max} \sim \mathrm{We}^{1/4}$ but $\beta_{max} \sim \mathrm{We}^{1/5}$, due to the similar dynamic behaviors between impacting nanodroplets and Hertz balls. Besides, the capillary regime is significantly reduced with We only ranging from 1 to ≈ 40. Once We exceeds the narrow capillary regime, the impacting nanodroplet falls into the crossover regime (which is also called transition regime), in which the droplet is controlled not only by inertial and capillary forces but also viscous force, and satisfies another scaling law of $\beta_{max} \sim \mathrm{We}^{1/2}\mathrm{Oh}^{1/3}$.

Despite the progress in revisiting classical problems by studies above, flat surfaces are, in fact, ideal in a real impact process. Especially in the mentioned studies [22–25], even the impact dynamics on flat superhydrophobic surfaces was investigated by MD simulations. There, indeed, never exists a flat or intrinsic superhydrophobic surface, and decorating a flat surface with textures is the only way to get a superhydrophobic surface [36]. The previous studies on millimeter-sized droplets frequently ignored the effect of textures and considered the superhydrophobic surfaces as flat ones with high intrinsic contact angles, which is ascribed to the condition that the size ratio of textures to millimeter-sized droplets is extremely small [8–10,37]. However, the feature

sizes of textures and nanodroplets are comparable so at the nanoscale, textured surfaces should be considered as specific objects in the research of impact dynamics instead of arbitrarily simplifying them as flat surfaces with high contact angles.

To match practical impact processes, instead of ideal flat surfaces, certain recent studies focused on nanodroplets impacting pillared surfaces [38–41]. Here, three texture parameters, h, w (or p), and ϕ, are additionally required to comprehensively describe the impact dynamics, where h, w, p, and $\varphi(= w^2/p^2)$ are the height of pillars, the width of pillars, the distance between pillars, and the solid fraction of pillars, respectively. On pillared surfaces, the classical problems (identifying outcome regimes and modeling $\beta_{\max}$) are further revisited. The first crucial mechanism for both millimeter-sized and nanoscale impacting droplets on pillared surfaces is that there exist two wetting states of droplets, i.e., the Cassie and Wenzel states, and the wetting transition between the two states may occur during impact, adding the complexity of impact dynamics. In this work, the Cassie-to-Wenzel wetting transition and Wenzel-to-Cassie dewetting transition are referred to as wetting transition and dewetting transition, respectively, for better readability. Lv *et al.* [39] emphasized a second mechanism especially for impacting nanodroplets on pillared surfaces. For millimeter-sized droplets impacting surfaces with nanopillars, the volume ratio of the intruding liquid to the entire droplet is negligible. However, this ratio is no longer negligible for nanodroplets because of violent intrusion in pillars with comparable sizes of nanodroplets. Consequently, the energy dissipation mechanism alters with the initial kinetic energy being dissipated not only by the violent internal flow inside the bulk droplet atop pillars but also by the liquid intruding into pillar gaps. Therefore, they inferred that bouncing is impossible to take place when impacting nanodroplets experience the wetting transition because of the huge dissipation by overcoming the energy barrier of the dewetting transition and the enhanced viscous dissipation of the liquid intruding into pillar gaps. On the basis of this insight, they stated that there only exist four outcomes for nanodroplets on pillared surfaces, i.e., first sticky (1S), first nonbouncing (1NB), second nonbouncing (2NB), and first bouncing (1B), whose schematics and descriptions are shown in Fig. 1. Here, the naming of sticky, nonbouncing, and bouncing, representing the eventual state of impacting nanodroplets, follows the previous studies [42,43]; the naming of first and second stands for the wetting transition feature.

Despite a phase diagram being constructed by Lv *et al.* [39], which claimed that the outcome regimes on pillared surfaces have been comprehensively identified, the basal mechanism that intrusion would enhance viscous dissipation is worth the doubt. Indeed, the viscous dissipation must take place in pillar gaps; however, it is possibly not significantly enhanced for the following several reasons. First, as liquid intrudes into pillar gaps, the sidewalls are wetted, which is a free-energy-increasing process and thereby indicates that the kinetic energy of the intruding liquid is not all dissipated to heat but is partly stored as surface energy, provided that the intrinsic wettability of the sidewalls is hydrophobic. Second, the no-slip condition is violated at the nanoscale [28], and therefore, the shear flow effect is reduced, which also adds to the possibility that the viscous dissipation in the narrow pillar gaps is weakened. If the liquid intrusion effect does not enhance the viscous dissipation significantly, an impacting nanodroplet after experiencing the wetting transition still probably has enough energy to achieve the dewetting transition and even bounce off a pillared surface. Thus, the second sticky (2S) and the second bouncing (2B), as shown in Fig. 1, are still possible to be observed. A piece of evidence has recently been provided by the study of Gao *et al.* [38] that the 2B outcome indeed appeared at a large enough We. As a result, the phase diagram developed by Lv *et al.* [39] does not contain all outcome regimes, and hence it needs to be reconstructed in wider ranges of Weber numbers, intrinsic surface wettability, and pillar geometry. Additionally, the reconstruction of regime diagrams also helps us to further clarify the dissipation mechanism occurring in pillar gaps and its effect on the impact dynamics of nanodroplets.

The other classical problem of modeling $\beta_{\max}$ for nanodroplets impacting pillared surfaces has been revisited by recent studies [38,40]. Herein, new physical insights into the liquid intrusion effect are desired to obtain by referring to the models. However, in their theoretical modeling, impacting nanodroplets are assumed to be perfect Cassie droplets throughout the whole impact process, which indicates that no liquid intrudes into pillar gaps and the nanodroplets only contact with the tops

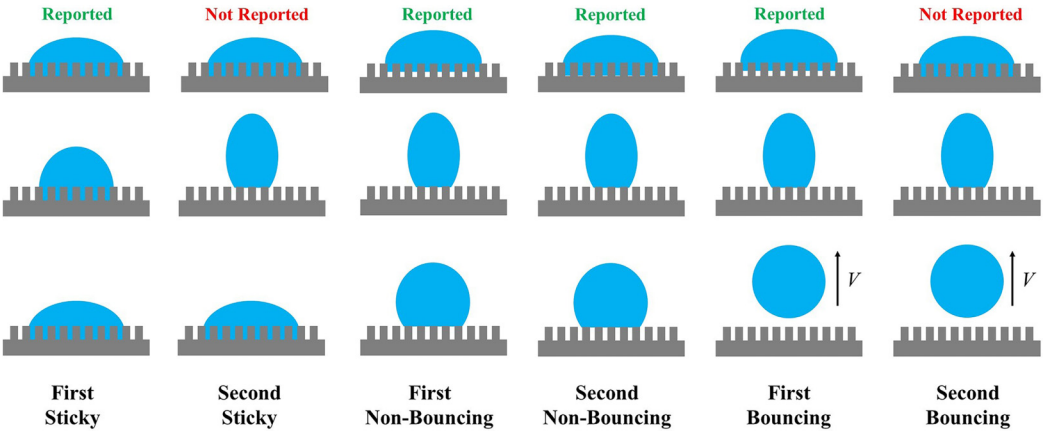

FIG. 1. The schematics of all possible outcomes for impacting nanodroplets on pillared surfaces, where each outcome is described by three subfigures representing the maximum spreading state, the typical middle state between the maximum spreading and final states, and the final state, respectively. The first sticky (1S) notes that a nanodroplet experiences the wetting transition and is not able to transition back to the Cassie state; the second sticky (2S) represents that the one experiences the dewetting transition after the wetting transition but subsequently falls back to the Wenzel state. The first nonbouncing (1NB) stands for a nanodroplet neither experiencing the wetting transition nor bouncing off surfaces; the second nonbouncing (2NB) shows that a nanodroplet experiences the wetting transition and then returns to and stays in the Cassie state. The first bouncing (1B) illustrates that an eventually bouncing nanodroplet does not experience the wetting transition, while the second bouncing (2B) displays the finally bouncing nanodroplet that experiences both the wetting transition and the dewetting transition before bouncing.

of pillars. As a result, the solid-liquid interfacial area is modified by the solid fraction, ϕ, for estimating the surface energy in their models. This assumption is acceptable for millimeter-sized impacting droplets because the intrusion volume of liquid is small enough compared with the initial droplet volume, which would not yield significantly distinct dynamic behaviors during spreading. Nonetheless, the wetting transition can be triggered even if impact takes place at a low We of 8.24 at the nanoscale [38]; thus, the liquid intrusion effect must be taken into account for impacting nanodroplets on pillared surfaces due to the large ratio of the intrusion volume to the initial volume of nanodroplets. Within this context, the existing models ignore the possible wetting transition and thus do not present the intrusion effect; accordingly, they may not be able to predict $\beta_{\max}$ of impacting nanodroplets on pillared surfaces accurately when liquid intrusion is violent. Despite both of the studies implementing the comparison between their models and MD results for claiming the effectiveness of their models, only a set of data of impact on a pillared surface with fixed parameters is used in each comparison, and therefore these models are not proven universal. As a result, all current models of $\beta_{\max}$ are far from satisfactory for interpreting the liquid intrusion effect on the impact dynamics of nanodroplets on pillared surfaces.

Furthermore, it should be noted that the impacting nanodroplet has an unimaginably large impact velocity at a similar Weber number with millimeter-sized droplets. For instance, as reported in a real nanoscale printing, an impacting nanodroplet can have an extremely large impact velocity at $\approx$250 m s^{-1} when We $\approx$ 105 [18], indicating a correspondingly large Mach number (Ma $= V_0/U_s$) of $\approx$0.74, where U_s is the speed of sound. Zhang *et al.* [14] investigated the impact of argon nanodroplets in an environment filled with argon vapor, reporting that the droplet volume can be compressed by $\approx$0.82% at Ma $\approx$ 0.1. Based on this observation, they inferred that the volume variation can rise to 7% at Ma $= 0.24$, which becomes worrisome. If this insight holds true, in addition to the effect of solid surfaces, the impact dynamics of nanodroplets should be controlled by

TABLE I. Simulation series list with descriptions of parametric ranges for each series.

Series	Description ($L = 1.96$ Å)	We and h ranges
1	$\varphi = 44\%$, $w = 8L$, $\theta = 105^\circ$, $P = 0$	
2	$\varphi = 44\%$, $w = 8L$, $\theta = 85^\circ$, $P = 0$	
3	$\varphi = 44\%$, $w = 8L$, $\theta = 125^\circ$, $P = 0$	We in 1.51 to 109.03
4	$\varphi = 44\%$, $w = 4L$, $\theta = 105^\circ$, $P = 0$	h in $0L$ to $22L$ with interval of $2L$
5	$\varphi = 25\%$, $w = 4L$, $\theta = 105^\circ$, $P = 0$	
6	$\varphi = 44\%$, $w = 8L$, $\theta = 105^\circ$, $P \approx 1$ atm (filled N_2)	

not only We and Oh (or Re) but also Ma. However, Galliker *et al.* [18] reported that the maximum spreading factor is still expected to be predicted only by We and Re according to experiments. Recent simulation studies on the maximum spreading factor also do not report the compressibility effect as well. For example, Y. B. Wang *et al.* [23] and Y.-F. Wang *et al.* [22] considered both a water nanodroplet system (nearly no gas) and an argon nanodroplet system (around by argon vapor) and found the maximum spreading factor is identical for both water and argon nanodroplets when We, Oh, and θ are the same. In this work, more simulations are expected to validate that the compressibility effect indeed does not take place for impacts of nanodroplets at $O(100\,\mathrm{m\,s^{-1}})$, and the underlying reason for the absence of the compressibility effect will also be discussed with the help of simulations and literature.

This work investigates a nanodroplet impacting a pillared surface, aiming to identify outcome regimes and model $\beta_{\max}$. Six series of simulations covering wide parametric ranges of We, Oh, θ, h, w, ϕ, and P (gas pressure), as shown in Table I, comprehensively reveal outcome regimes. Each series can reveal outcomes in wide ranges of We and h, and comparing pairs of series data can reveal the effect of other surface parameters (θ, w, ϕ, and P). It should be noted that, compared with no additional gas molecules in series 1–5, the simulation system in series 6 is filled with N_2 for investigating the effect of gas surrounding nanodroplets. Subsequently, the boundaries of outcome regimes are established for developing a universal phase diagram. With the help of the criteria of boundaries, the dissipation mechanism occurring in pillar gaps and its effect on the impact dynamics of nanodroplets can be effectively understood. In modeling $\beta_{\max}$, understanding the detailed intrusion morphology of liquid is important when impacting on pillared surfaces. The intrusion regimes are classified by different intrusion morphology, and the scalings of intrusion volume in different intrusion regimes and the corresponding transition criterion are both established. Combining the scalings of intrusion volume with the scaling laws of $\beta_{\max}$ on flat surfaces leads to the new scaling laws of $\beta_{\max}$ on pillared surfaces.

II. SIMULATION METHOD

All simulations are implemented by the LAMMPS (large-scale atomic/molecular massively parallel simulation) package. Figure 2(a) shows the schematics of the simulation system for an impacting nanodroplet on a pillared surface in a box with dimensions $34\times34\times23\,\mathrm{nm}^3$. Periodic boundary conditions are applied to the x and y directions and a fixed boundary condition is applied to the z direction. The pillar parameters, including the height of pillars, h, the width of pillars, w, and the pitch between pillars, p, are exhibited in Fig. 2(b). The nanodroplet and the substrate in the simulation system are generated, using the face-centered-cubic alignment. The lattice constant for the substrate is $a = 3.92$ Å and a typical length $L = a/2 = 1.96$ Å is adopted for evaluating the sizes of pillar parameters later. In a real nanoscale printing process, the substrate does not deform, and therefore, a virtual spring is imposed on each solid atom to its initial position to avoid possible deformation of the substrate. The nanodroplet has a diameter of 10 nm and contains 17 474 water molecules. Initially, the droplet and the substrate are separated by 1.8 nm to avoid possible

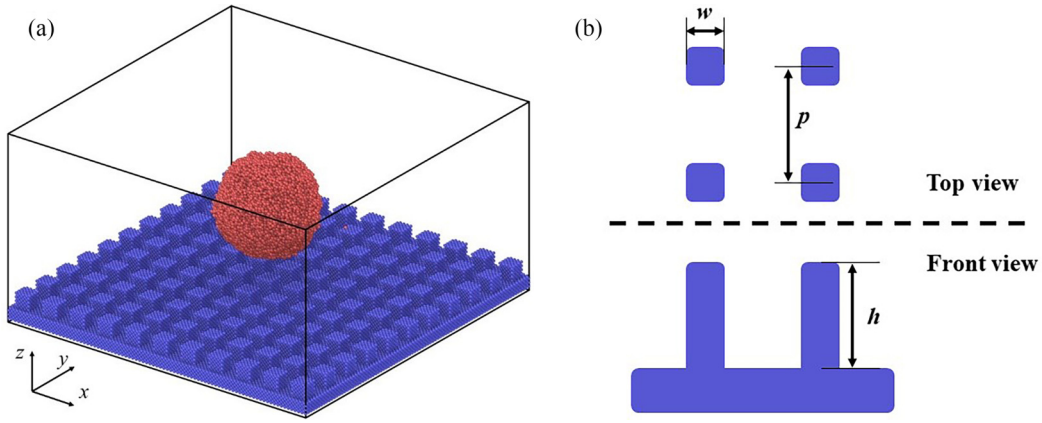

FIG. 2. The schematics of (a) the simulation system and (b) the pillar parameters, where h, w, and p, are the height of pillars, the width of pillars, and the pitch between pillars, respectively.

interactions between them before impact. This separation distance is identical for all cases in this work.

The monatomic water (mW) model, derived from the Stillinger-Weber silicon potential, describes the interactions between water molecules [44]. As a coarse-grained model, the mW model can significantly improve computational efficiency. Besides, the model can also accurately reproduce most physical properties of water, such as surface tension, density, energetics, and others. However, owing to the exclusion of the reorientation of hydrogen atoms, the viscosity of this model is three times lower than the experimental value of water [44]. As tested by the previous study [44], the properties of mW are $\rho = 996\,\mathrm{kg\,m^3}$, $\gamma = 0.066\,\mathrm{N\,m^{-1}}$, and $\mu = 851/3 = 283.7\,\mu\mathrm{Pa\,s}$, which are used to calculated We and Oh.

The interactions for s-s (solid atoms) and s-l (solid atoms and mW molecules) pairs are described by the Lennard-Jones 12–6 potential model, expressed as

$$U(r) = 4\varepsilon\left[\left(\frac{\sigma}{r}\right)^{12} - \left(\frac{\sigma}{r}\right)^{6}\right], \tag{1}$$

where r is the distance of the atom pairs, ε is the depth of the potential well, σ is the zero-crossing distance, and r_{cut} is the cutoff distance which is adopted as 1 nm. In this work, the parameters, $\varepsilon_{\mathrm{s\text{-}s}}$, $\sigma_{\mathrm{s\text{-}s}}$, and $\sigma_{\mathrm{s\text{-}l}}$, are fixed as 0.69375 eV, 0.247 nm, and 0.28155 nm, respectively [23]. The energy parameter, $\varepsilon_{\mathrm{s\text{-}l}}$, is considered to be an adjustable parameter for producing different intrinsic wettability. The relationship between the intrinsic contact angle and the adjustable parameter, $\varepsilon_{\mathrm{s\text{-}l}}$, can be evaluated by placing a nanodroplet on a flat surface and estimating the contact angle after the nanodroplet reaches equilibrium. With the help of calculating the time-average density profile, the surface of droplets can be identified using a density threshold that is half of the liquid-phase density. Subsequently, by circle fitting on the surface of droplets, the contact angle of droplets at $\varepsilon_{\mathrm{s\text{-}l}}$ is obtained by measuring the angle at the three-phase contact line. Based on this method, the contact angles $\theta = 85^\circ$, 105°, and 125° correspond to $\varepsilon_{\mathrm{s\text{-}l}} = 0.0137$, 0.0102, and 0.0068 eV, respectively [23].

No additional gas molecules are added in the simulation system in series 1–5, whereas N_2 molecules are added to achieve $P = 1$ atm for investigating the effect of ambient gas on impacting nanodroplets at an ordinary pressure in series 6. The interaction parameters between nitrogen atoms are set as $\varepsilon_{\mathrm{g\text{-}g}} = 0.0073$ eV and $\sigma_{\mathrm{g\text{-}g}} = 0.371$ nm [45]. Each nitrogen molecule consists of two nitrogen atoms connected by a fixed chemical bond. The interaction parameters for s-g (solid and gas atoms) and l-g (mW molecules and gas atoms) are $\varepsilon_{\mathrm{s\text{-}g}} = 0.0386$ eV, $\sigma_{\mathrm{s\text{-}g}} = 0.335$ nm, $\varepsilon_{\mathrm{l\text{-}g}} = 0.0063$ eV, and $\sigma_{\mathrm{l\text{-}g}} = 0.349$ nm.

MD simulations are launched with a time step of 2 fs. The equilibrium process runs in the *N-V-T* ensemble (canonical ensemble) with relaxation for 2 ns and the center of mass of the nanodroplet is fixed in the whole process. Using the Nosé-Hoover thermostat, the system temperature T is controlled at 300 K. After reaching equilibrium, running in the *N-V-E* ensemble (microcanonical ensemble), an additional velocity (V_0) along the negative z direction is imposed to the nanodroplet to impact. The position and velocity of each mW molecule are recorded with an interval of 1 ps for further analysis.

For validating the effectiveness of mW in investigating the impact dynamics of nanodroplets, impacts by argon nanodroplets simulated by the Lennard-Jones 12–6 potential model are also implemented. As shown in Fig. S1 of the Supplemental Material [46], the maximum spreading factor shows the same for both impacts of water and argon nanodroplets on flat surfaces, showing the same effectiveness of this coarse-grained model as the full-atom model.

III. OUTCOME REGIMES

A. Effect of pillar height

In this section, the cases in series 1 (fixed $\varphi = 44\%$, $w = 8L$, and $\theta = 105^\circ$) are used for revealing the effect of pillar height (h) and We. Since h significantly affects liquid intrusion and also generates distinct wetting features of surfaces, the outcome regimes of impacting nanodroplets are discussed in two h-dependent groups: a low-h range ($0 \leqslant h \leqslant 4L$) and a high-$h$ range ($6L \leqslant h \leqslant 22L$).

In the low-h range ($0 \leqslant h \leqslant 4L$), tested by a sessile droplet, all surfaces are found to favor the Wenzel state; i.e., the droplet must equilibrate in the Wenzel state eventually regardless of its initial wetting state being the Cassie or the Wenzel state. Thus, the Wenzel state is the globally minimum energy state. Frequently, a surface with such a wetting feature is termed a Wenzel surface. Nonetheless, it should be emphasized that the mechanism of the Wenzel surface at the nanoscale is different from the one at the macroscale. At the macroscale, no matter how short the pillars are, liquid could not spontaneously intrude into the pillar gaps to achieve the Wenzel state, provided that the intrinsic wettability is hydrophobic. This is because the intrusion process for a sessile droplet before the liquid touching the basal wall is a free-energy-increasing process according to the macroscopic interfacial thermodynamics [47]. However, at the nanoscale, the extremely small pillars render the liquid intrusion process spontaneous [48], which is possibly ascribed to the fact that, before the liquid touches the basal wall, there has existed intermolecular attractive interactions between the liquid and the basal wall, because the range of pillar height (from 0.392 to 0.784 nm) discussed here is lower than the effective length of the van der Waals force [49]. As a result, the liquid intrusion process can be free-energy decreasing and the pillared surfaces with enough low h are Wenzel surfaces, despite the intrinsic wettability being hydrophobic.

The schematic of a free-energy-change path for a Wenzel surface is drawn in Fig. 3(a), based on our previous work for nanoscale wetting transition on pillared surfaces [50]. On Wenzel surfaces, there exists a spontaneously decreasing free energy path from the Cassie to the Wenzel state so that an impacting nanodroplet would spread to the maximum spreading state with the inevitable wetting transition (A $\rightarrow$ B $\rightarrow$ C), noting the possible 1S, 2S, and 2B regimes but impossible 1B, 1NB, and 2NB regimes on Wenzel surfaces. At the maximum spreading state, all available kinetic energy after overcoming the viscous dissipation during spreading is stored as surface energy. As an impacting nanodroplet starts to retract by releasing the surface energy, there exists an energy barrier (ΔF_{CW}) resisting the dewetting from the Wenzel to the Cassie state, as shown in Fig. 3(a). Besides, even if the impacting nanodroplet returns to the Cassie state, there is still another energy barrier (ΔF_{CB}) to hinder the bouncing, due to the adhesion between liquid and surface. By comparing the available energy at the maximum spreading state with the energy barriers (ΔF_{CB} and ΔF_{CW}), three possible outcome regimes could be speculated. If the initial kinetic energy of a nanodroplet is low, the available energy stored at the maximum spreading state is correspondingly low, so that the nanodroplet is not able to overcome ΔF_{CW} and, finally, equilibrates in the Wenzel state

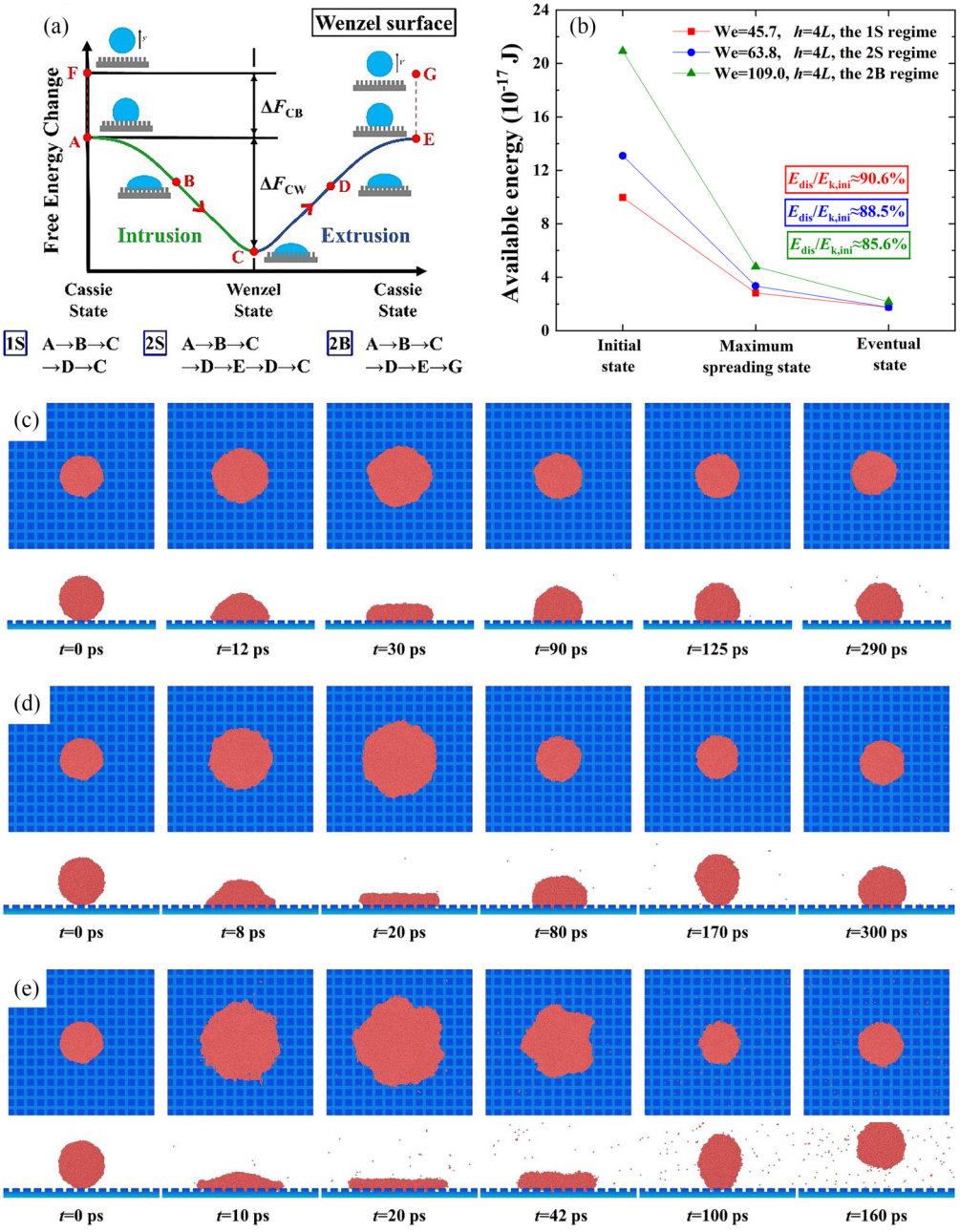

FIG. 3. (a) The schematic of the free-energy-change path on Wenzel surfaces; (b) the extracted available energy at important states, where the corresponding calculation method is shown in the Supplemental Material [46]; and snapshots of nanodroplets with Oh = 0.35 impacting pillared surfaces with $h = 4L$ at (c) We = 45.7, (d) We = 63.8, and (e) We = 109.0, showing the impacting nanodroplets in the 1S, 2S, and 2B regimes, respectively.

(C → D → C), showing the 1S regime. With intermediate initial kinetic energy, the nanodroplet has more available energy at the maximum spreading state, and the dewetting transition is desired to complete (C → D → E). At this time, if there is no sufficient residual energy to overcome ΔF_{CB}, the

nanodroplet will finally transition back and equilibrate in the Wenzel state (E → D → C), noting the 2S regime. When the initial kinetic energy is high enough, there still exists enough residual energy to overcome the adhesion after completing the dewetting transition (C → D → E → G), illustrating the 2B regime. In summary, there theoretically exist three possible outcome regimes on Wenzel surfaces, i.e., 1S, 2S, and 2B regimes.

With the assistance of extracted available energy (kinetic energy plus surface energy) from MD simulations at important states, i.e., the initial, maximum spreading, and eventual states, as shown in Fig. 3(b), the outcomes on Wenzel surfaces are analyzed, where E_{dis} in the figure represents the viscous dissipation during spreading. As shown in Fig. 3(c), on pillared surfaces with $h = 4L$ at We = 45.7, the nanodroplet spreads to the maximum state at $t = 30$ ps with the wetting transition. Due to the relatively low initial kinetic energy, the stored energy at the maximum spreading state is also small, as shown in Fig. 3(b), so that the nanodroplet is slightly lifted at the end of the retraction and finally stays in the Wenzel state, showing the occurrence of the 1S regime. Among all possible outcome regimes (1S, 2S, and 2B regimes) on Wenzel surfaces, Lv *et al.* [39] claimed that the enhanced viscous dissipation due to the liquid intrusion effect and the huge energy barrier, ΔF_{CW}, render the 2S and 2B regimes impossible to take place, and there should only exist the 1S regime. However, the viscous dissipation in pillar gaps may not be significantly larger than the one in the bulk droplet because the significant slip has been reported for impacts of nanodroplets, reducing the viscous dissipation in pillar gaps. The intrusion volume of liquid must increase with velocity; however, the energy budget shows that the viscous dissipation proportion to the initial kinetic energy decreases with increasing velocity, as shown in Fig. 3(b), which provides the evidence for the statement that the velocity gradients in pillar gaps are possibly weaker than the ones in the bulk droplet on Wenzel surfaces. On the other hand, the energy barrier for the dewetting transition is not infinite but is determined by surface parameters (θ, h, w, and ϕ); once all the parameters are fixed, the energy barrier is constant. Therefore, increasing the initial kinetic energy can always enlarge the available energy at the maximum spreading state for possibly overcoming ΔF_{CW}. As shown in Figs. 3(b) and 3(d), at a larger We of 63.8, the impacting nanodroplet forms a thinner cylinder shape with larger available energy at the maximum spreading state. As expected, the nanodroplet has a more significant upward motion than the one at We = 45.7 at the end of retraction ($t = 170$ ps) and the dewetting transition is achieved. Nonetheless, there is no more residual energy at the end of retraction and, thereby, the nanodroplet returns to the Wenzel state and equilibrates eventually, showing the emerged 2S regime. Fortunately, despite no bouncing behavior taking place at such We, the contact area between the liquid and the top surface has become extremely low when the dewetting transition is completed ($t = 170$ ps), implying that even the 2B regime is desired to occur on Wenzel surfaces if We is further increased. As anticipated, at an extremely large We of 109.0, enough available energy at the maximum spreading state not only promotes the dewetting transition but also subsequently triggers the bouncing, as shown in Fig. 3(e), showing the occurrence of the 2B regime.

In the high-h range ($6L \leqslant h \leqslant 22L$), the surfaces prefer the Cassie state. Such surfaces have globally minimum energy in the Cassie state; i.e., no matter whether a sessile droplet is in the Cassie or the Wenzel state initially, it would finally equilibrate to the Cassie state. Accordingly, they are referred to as Cassie surfaces. The free-energy-change path for a droplet on a Cassie surface is illustrated in Fig. 4(a). In comparison with the existing energy barrier for the dewetting transition on a Wenzel surface, here the energy barrier on a Cassie surface is altered to resist the wetting transition. An impacting nanodroplet possibly fails to achieve the wetting transition (low We, A → B → A) or experiences the wetting transition and spontaneously transitions back to the Cassie state (high We, A → B → C → D → E). For each possible process above, the nanodroplet can either equilibrate in the Cassie state (low We, no further motion) or bounce off surfaces (high We, A → F or E → G). Combining them in pairs, there theoretically exist four possible outcome regimes, i.e., 1NB, 1B, 2NB, and 2B regimes, on Cassie surfaces.

With the help of the extracted available energy shown in Fig. 4(b), the outcomes on Cassie surfaces are discussed, where E_{dis} in the figure stands for the viscous dissipation during spreading.

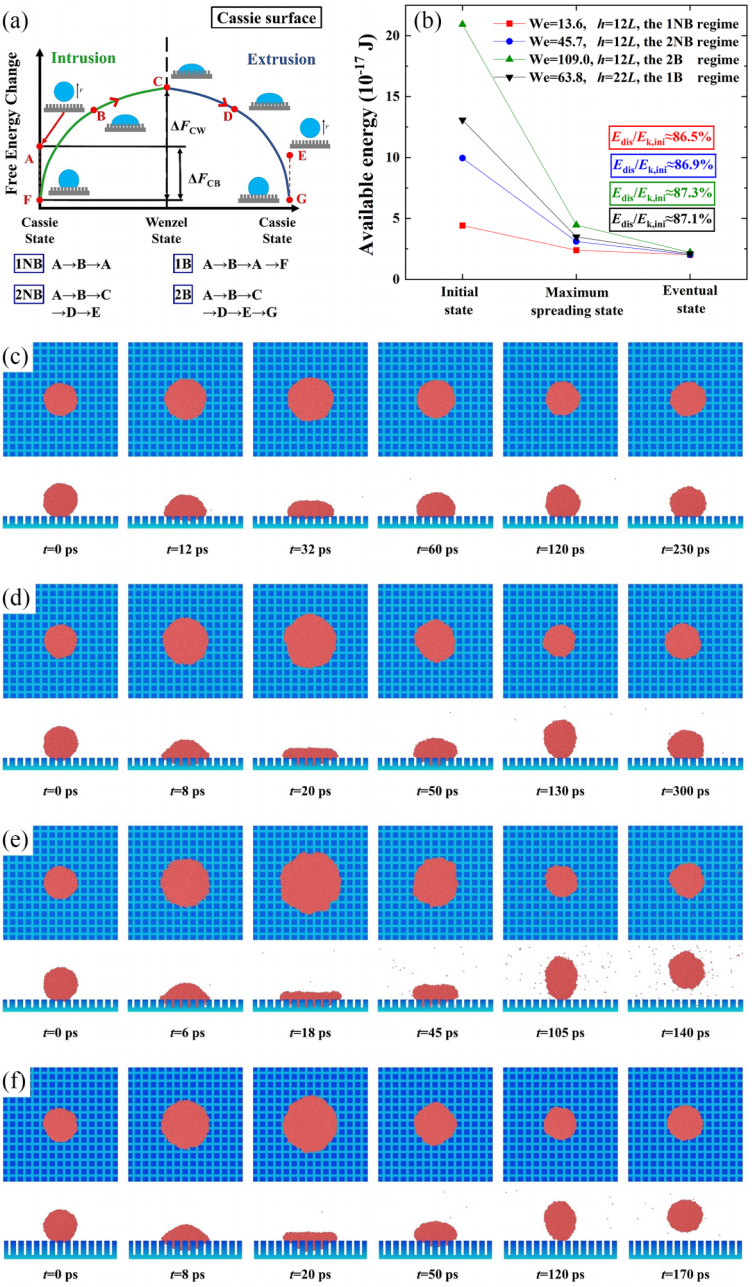

FIG. 4. (a) The schematic of the free-energy-change path on Cassie surfaces; (b) the extracted available energy at important states, where the corresponding calculation method is shown in the Supplemental Material [46]; snapshots of nanodroplets with Oh = 0.35 impacting pillared surfaces with $h = 12L$ at (c) We = 13.6, (d) We = 45.7, and (e) We = 109.0, showing the impacting nanodroplets in the 1NB, 2NB, and 2B regimes, respectively; and (f) snapshots of a nanodroplet with Oh = 0.35 impacting a pillared surface with $h = 22L$ at We = 63.8, noting the impacting nanodroplet in the 1B regime.

On a pillared surface with $h = 12L$, the nanodroplet with low initial kinetic energy is not able to achieve the wetting transition, so it remains on the top of surfaces and eventually equilibrates in the Cassie state, as shown in Fig. 4(c), indicating the occurrence of the 1NB regime. With an increased We of 45.7, the nanodroplet has more initial kinetic energy so the wetting transition is successfully triggered; subsequently, it spontaneously transitions back to the Cassie state but no bouncing behavior is observed, as shown in Fig. 4(d), demonstrating the presence of the 2NB regime. Lv *et al.* [39] discussed that despite no extra energy being required to complete the dewetting transition on Cassie surfaces, most of the initial kinetic energy has been used during the wetting transition so the bouncing behavior could not take place after completing the dewetting transition. On the basis of this insight, they claimed that the 2B regime could not occur on Cassie surfaces. However, it is possible that they exaggerated the viscous dissipation by the liquid intrusion as discussed on Wenzel surfaces before. Compared with pillared surfaces with low h (for which the 2B regime has been observed), impacting nanodroplets store surface energy more easily during spreading by the liquid intrusion when h is increased. For instance, an impacting nanodroplet can dissipate 90.6% of the initial kinetic energy during spreading at $\mathrm{We} = 45.7$ and $h = 4L$, as shown in Fig. 3(b), whereas only 86.9% of the initial kinetic energy is dissipated at the same Weber number when h is increased to $12L$, as shown in Fig. 4(b), showing more initial kinetic energy is stored as surface energy instead of being dissipated. As a result, more violent liquid intrusion does not strongly enhance the viscous dissipation during spreading, and no doubt, the 2B regime is still possible to exist on Cassie surfaces in high-We ranges. As anticipated, at a high We of 109.0, although the nanodroplet undergoes both the wetting transition and the spontaneous dewetting transition, it bounces off a surface eventually, presenting the 2B regime [Fig. 4(e)]. Herein, the 1NB, 2NB, and 2B regimes are successfully observed for impacting nanodroplets on pillared surfaces with $h = 12L$. However, the 1B regime does not appear at this h. This can be ascribed to the fact that the energy barrier for the wetting transition is relatively lower than the one of adhesion so the nanodroplet prefers the wetting transition compared with the direct bouncing. It is well recognized that increasing h can enlarge the energy barrier for the wetting transition [50], provided that the intrinsic wettability is hydrophobic. Thus, when h is large enough, the energy barrier for the wetting transition can exceed the one of adhesion, and hence the nanodroplet prefers bouncing instead of the wetting transition. As expected, Fig. 4(f) shows that when impacting the pillared surface with a larger h of $22L$, the nanodroplet directly bounces off the surface without the wetting transition at $\mathrm{We} = 63.8$, showing the presence of the 1B regime. In summary, all theoretical outcome regimes are observed with the 1S, 2S, and 2B regimes on Wenzel surfaces and the 1NB, 1B, 2NB, and 2B regimes on Cassie surfaces.

By testing the wide We range, the richer outcome regimes compared with Lv *et al.* [39] are identified with a total of six outcome regimes that are drawn in Fig. 5 as a phase diagram. On Wenzel surfaces, there are 1S, 2S, and 2B regimes. The 1S-2S boundary is characterized by the dewetting transition; the 2S-2B boundary is determined by bouncing on Wenzel surfaces. On Cassie surfaces, 1NB, 1B, 2NB, and 2B regimes are observed; however, only two boundaries separate the four regimes. The first is referred to as the wetting transition boundary and the second is termed the bouncing boundary on Cassie surfaces. Specifically, the wetting transition boundary separates the 1B and 1NB regimes from the 2B and 2NB regimes, whereas the bouncing boundary on Cassie surfaces distinguishes the 1NB and 2NB regimes from the 1B and 2B regimes. Briefly, four boundaries, i.e., the 1S-2S boundary and the 2S-2B boundary on Wenzel surfaces, as well as the wetting transition boundary and the bouncing boundary on Cassie surfaces, separate all six outcome regimes.

Focusing on the wetting transition boundary, the relationship between $\mathrm{We}_{\mathrm{cri,C\text{-}W}}$ and surface parameters (θ, h, w, ϕ) is desired to be obtained, where $\mathrm{We}_{\mathrm{cri,C\text{-}W}}$ is the critical Weber number for trigging the wetting transition on Cassie surfaces. In an intrusion process, the intruding depth of the liquid at the initial impact point is always the deepest and, once it touches the basal wall, the wetting transition is achieved; thus, this deepest depth of the intruding liquid (h_{i}) is considered for revealing the wetting transition. Herein, the volume of the intruding liquid that would suffer

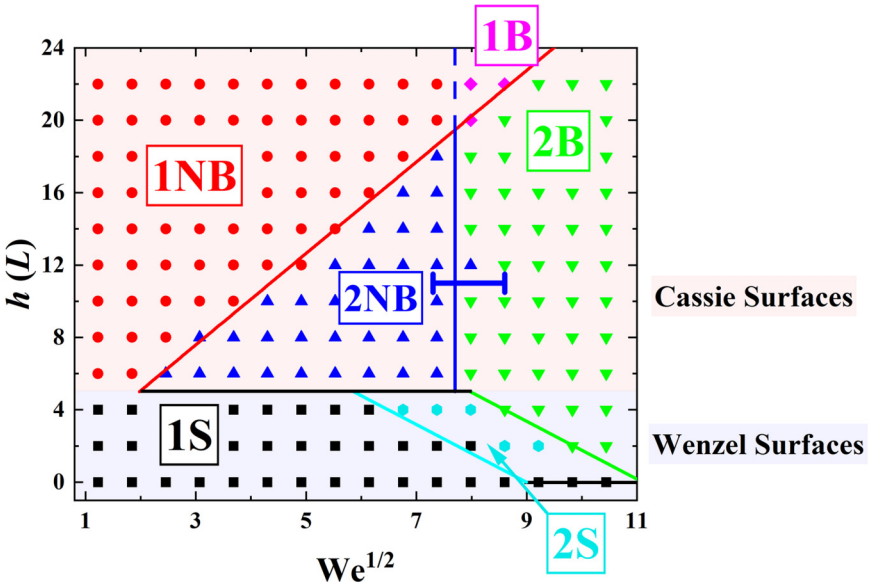

FIG. 5. Phase diagram of nanodroplets with Oh = 0.35 impacting pillared surfaces with wide ranges of h and We. Here, the red, green, and cyan solid lines and the blue bar represent the prediction results of Eqs. (6), (11), and (14) and Eq. (12), respectively. The blue solid line stands for the real bouncing boundary on Cassie surfaces.

a strong resistance (capillary force) of $F_c \sim \gamma w \cos\theta$ is $\Omega_i \sim (p^2/D_0^2)D_0^3 = p^2 D_0$. Therefore, the acceleration of the liquid can be expressed as

$$\alpha_i = (F_c/\rho\Omega_i) \sim \gamma\varphi\cos\theta/(\rho w D_0). \tag{2}$$

Besides, another expression of α_i which includes V_0 and h_i is obtained from the kinematic view,

$$\alpha_i \sim -V_0/t_i, \tag{3}$$

where t_i is the intrusion time, i.e., the time span from the beginning to the end of intrusion. In s previous study [37], the characteristic time for an impact process dominated by inertial and capillary forces is $D_0/V_0(\mathrm{We}^{1/2})$, i.e., the famous inertial-capillary time, where the initial diameter, D_0, is the characteristic length. However, the intrusion time does not simply scale as $D_0/V_0(\mathrm{We}^{1/2})$ because it should also rely on another characteristic length, i.e., h_i. Intrusion takes place during the spreading process of the droplet. When the intrusion length is small compared with the droplet diameter, the intrusion time is significantly shorter than the spreading time; while the intrusion length is comparable with the droplet diameter, the intrusion time also becomes comparable with the spreading time. Based on this analysis, the intrusion time can scale as the scale ratio, h_i/D_0, multiplied by the spreading time. For the spreading of impacting droplets, the timescale is determined by the inertial-capillary time ($\sim \mathrm{We}^{1/2} D_0/V_0$). Therefore, the intrusion time, t_i, eventually scales as $(h_i/D_0)\times(\mathrm{We}^{1/2} D_0/V_0)$, i.e., $t_i \sim h_i/V_0 \mathrm{We}^{1/2}$. Using this timescale, the kinematic expression of α_i is obtained as

$$\alpha_i \sim -V_0^2/(\mathrm{We}^{1/2} h_i). \tag{4}$$

Combining Eqs. (2) and (4), the relationship among We, h_i, and other surface parameters (θ, w, and ϕ) is obtained as

$$\mathrm{We}^{1/2} \sim \varphi h_i/w(-\cos\theta). \tag{5}$$

Once h_i equals the actual height of pillars, the wetting transition takes place; thus, replacing We and h_i by $\mathrm{We}_{\mathrm{cri,C\text{-}W}}$ and h, the criterion of the wetting transition is obtained as

$$\mathrm{We}_{\mathrm{cri,C\text{-}W}}^{1/2} \sim \varphi h/w(-\cos\theta). \tag{6}$$

This scaling law is also derived by Lv *et al.* [39] and agrees with the present MD data with a prefactor of 27.5, as shown in Fig. 5.

On Cassie surfaces, the wetting transition needs to overcome an energy barrier but the dewetting transition is spontaneous; inversely, on Wenzel surfaces, achieving the dewetting transition would face an energy barrier, while the wetting transition is spontaneous. Increasing h can enhance the former energy barrier, leading to an increase in $\mathrm{We}_{\mathrm{cri,C\text{-}W}}$, whereas it would weaken the latter energy barrier, resulting in a decrease in $\mathrm{We}_{\mathrm{cri,W\text{-}C}}$, where $\mathrm{We}_{\mathrm{cri,W\text{-}C}}$ is the critical Weber number for trigging the dewetting transition on Wenzel surfaces [50]. Here, a simple assumption is proposed that, with increasing h, the rates of change in $\mathrm{We}_{\mathrm{cri,C\text{-}W}}$ and $\mathrm{We}_{\mathrm{cri,W\text{-}C}}$ are negatively correlated, i.e.,

$$\frac{\mathrm{d}}{\mathrm{d}h}\mathrm{We}_{\mathrm{cri,W\text{-}C}}^{1/2} \sim -\frac{\mathrm{d}}{\mathrm{d}h}\mathrm{We}_{\mathrm{cri,C\text{-}W}}^{1/2}. \tag{7}$$

Substituting Eq. (6) in Eq. (7) yields

$$\frac{\mathrm{d}}{\mathrm{d}h}\mathrm{We}_{\mathrm{cri,W\text{-}C}}^{1/2} \sim \varphi\cos\theta/w. \tag{8}$$

This shows agreement with Fig. 5 in which the critical Weber number on the 1S-2S boundary on Wenzel surfaces decreases with increasing h. Intriguingly, the 2S-2B boundary (i.e., the bouncing boundary on Wenzel surfaces) is parallel with the 1S-2S boundary, as shown in Fig. 5. This may be ascribed to the fact that, on Wenzel surfaces, the transition from the Cassie state to bouncing only requires to overcome the adhesion between the lifted Cassie nanodroplet and the top surface, like the impacting nanodroplet from $t = 100$ to 160 ps in Fig. 3(e). Therefore, the bouncing boundary on Wenzel surfaces also follows the same expression,

$$\frac{\mathrm{d}}{\mathrm{d}h}\mathrm{We}_{\mathrm{cri,W\text{-}B}}^{1/2} \sim \varphi\cos\theta/w, \tag{9}$$

where $\mathrm{We}_{\mathrm{cri,W\text{-}B}}$ is the critical Weber number for triggering bouncing on Wenzel surfaces. Integrating Eq. (9) leads to a complete expression as

$$\mathrm{We}_{\mathrm{cri,W\text{-}B}}^{1/2} - \mathrm{We}_{\mathrm{cri,W\text{-}B}}^{1/2}|_{h=0} \sim \varphi\cos\theta h/w, \tag{10}$$

where $\mathrm{We}_{\mathrm{cri,W\text{-}B}}|_{h=0}$ is the critical Weber number for triggering bouncing on flat surfaces. Ma *et al.* [24] have investigated the criterion of impacting nanodroplets on flat surfaces and obtained a prediction model as $\mathrm{We}_{\mathrm{cri,W\text{-}B}}|_{h=0} = 172 + 188\cos\theta$, where 172 and 188 are constant fitting parameters. Combining this model into Eq. (10), the criterion for the bouncing on Wenzel surfaces is obtained as

$$\left[\mathrm{We}_{\mathrm{cri,W\text{-}B}}^{1/2} - (172 + 188\cos\theta)^{1/2}\right] \sim \varphi\cos\theta h/w. \tag{11}$$

With a prefactor of 44, Eq. (11) shows good agreement with the actual boundary, as shown in Fig. 5.

It should be noted that the bouncing boundaries on Wenzel and Cassie surfaces intersect at the critical pillar height (h_c) separating the Wenzel and Cassie surfaces, and the bouncing boundary on Cassie surfaces is independent of h so that the criterion of it can be obtained by substituting h_c in Eq. (11), expressed as

$$\left[\mathrm{We}_{\mathrm{cri,C\text{-}B}}^{1/2} - (172 + 188\cos\theta)^{1/2}\right] \sim \varphi\cos\theta h_c/w, \tag{12}$$

where $\mathrm{We}_{\mathrm{cri,C\text{-}B}}$ is the critical Weber number for triggering the bouncing on Cassie surfaces. It could be inferred that h_c must be between $4L$ and $6L$ in series 1, and here, taking $h_c = 4L$ and $6L$ in

Eq. (12), respectively, upper and lower values of $We_{cri,C\text{-}B}^{1/2}$ are obtained as 7.3 and 8.6 (i.e., $We_{cri,C\text{-}B}$ equaling 53.3 and 74), which successfully covers the actual bouncing boundary on Cassie surfaces, as shown in Fig. 5.

Besides the bouncing boundary on Cassie surfaces, the criterion of the 1S-2S boundary can also be further expressed based on Eq. (11). As mentioned, the critical Weber number of bouncing on Wenzel surfaces is larger than the one of the dewetting transition due to the additional energy barrier of adhesion. As a result, $We_{cri,C\text{-}B}$ includes two parts, i.e., one part for triggering the dewetting transition ($We_{cri,W\text{-}C}$) and the other part for inducing the bouncing of the Cassie nanodroplet (We_{ad}). Therefore, Eq. (11) can be rewritten as

$$\left[We_{cri,W\text{-}C}^{1/2} + We_{ad}^{1/2} - (172 + 188\cos\theta)^{1/2}\right] \sim \varphi \cos\theta h/w. \tag{13}$$

Because the energy barrier of overcoming the adhesion must be proportional to the contact area between the lifted Cassie nanodroplet and the top surface, and the contact area strongly depends on the solid fraction (ϕ), the expression of $We_{ad}^{1/2}$ is assumed as $We_{ad}^{1/2} \sim \varphi$ with a prefactor of 4.8 by fitting. Finally, Eq. (13) is expressed as

$$\left[We_{cri,W\text{-}C}^{1/2} + 4.8\varphi - (172 + 188\cos\theta)^{1/2}\right] \sim \varphi \cos\theta h/w. \tag{14}$$

As anticipated, Eq. (14) also shows good agreement in Fig. 5.

The four scaling laws obtained above, i.e., Eqs. (6), (11), (12), and (14), have been compared with the boundaries in Fig. 5, showing good agreement between them, where Eq. (6) has a prefactor of 27.5 and others have a prefactor of 44. Thus, all outcome boundaries, including the 1S-2S boundary and the 2S-2B boundary on Wenzel surfaces, and the wetting transition boundary and the bouncing boundary on Cassie surfaces, are determined. Because the Weber number, intrinsic wettability, and pillar parameters (ϕ, h, and w, by which the topology of pillared surfaces can be determined) are included in these scaling laws, it is expected that they can be applied to other impact conditions.

B. Effect of other parameters

The outcome regimes and corresponding boundaries have been preliminarily revealed in the last section by data of series 1 with fixed parameters of $\theta = 105^\circ$, $w = 8L$, and $\varphi = 44\%$ and varied parameters of We and h. Although the phase diagram (Fig. 5) has covered all possible outcome regimes and the models of all boundaries of the regimes are established, the models have not been validated when changing θ, w, or ϕ. Therefore, the phase diagrams of other series simulations (series 3–6) are also constructed and illustrated in Fig. 6 for further tests. Here it is worth noting that all surfaces in series 2 ($\theta = 85^\circ$) are Wenzel surfaces, and additionally, all impact cases in this series fall in the 1S regime. This may be ascribed to the fact that the wetting process in pillar gaps on an intrinsic hydrophilic pillared surface is naturally free-energy decreasing according to the macroscopic interfacial thermodynamics [47] and such an intrinsic hydrophilic pillared surface can significantly increase the energy barrier from the Wenzel to the Cassie state, compared with an intrinsic hydrophobic pillared surface [50]. Therefore, series 2 is not drawn as a phase diagram for further analysis of outcome regimes. Comparing Fig. 5 with Figs. 6(a), 6(b), and 6(d) can highlight the effect of θ, w, and P, respectively; comparing Fig. 6(b) with Fig. 6(c) is able to reveal the effect of ϕ.

As shown in Figs. 6(a)–6(d), the proposed scaling laws predict most boundaries accurately; however, two failures are found. The first is the applicability of the scaling law of the wetting transition boundary when θ is altered. As the dashed line shown in Fig. 6(a), this scaling law shows a significant deviation from the actual wetting transition boundary. Unexpectedly, the actual wetting transition boundary in Fig. 6(a) is identical to that in Fig. 5, which indicates that the wetting transition is not significantly affected by the intrinsic contact angle, provided that the intrinsic wettability is hydrophobic. This phenomenon violates the proposed θ-incorporated scaling law of $We_{cri,C\text{-}W}^{1/2} \sim \varphi h/w(-\cos\theta)$. A possible reason is that, during liquid intrusion, the capillary force

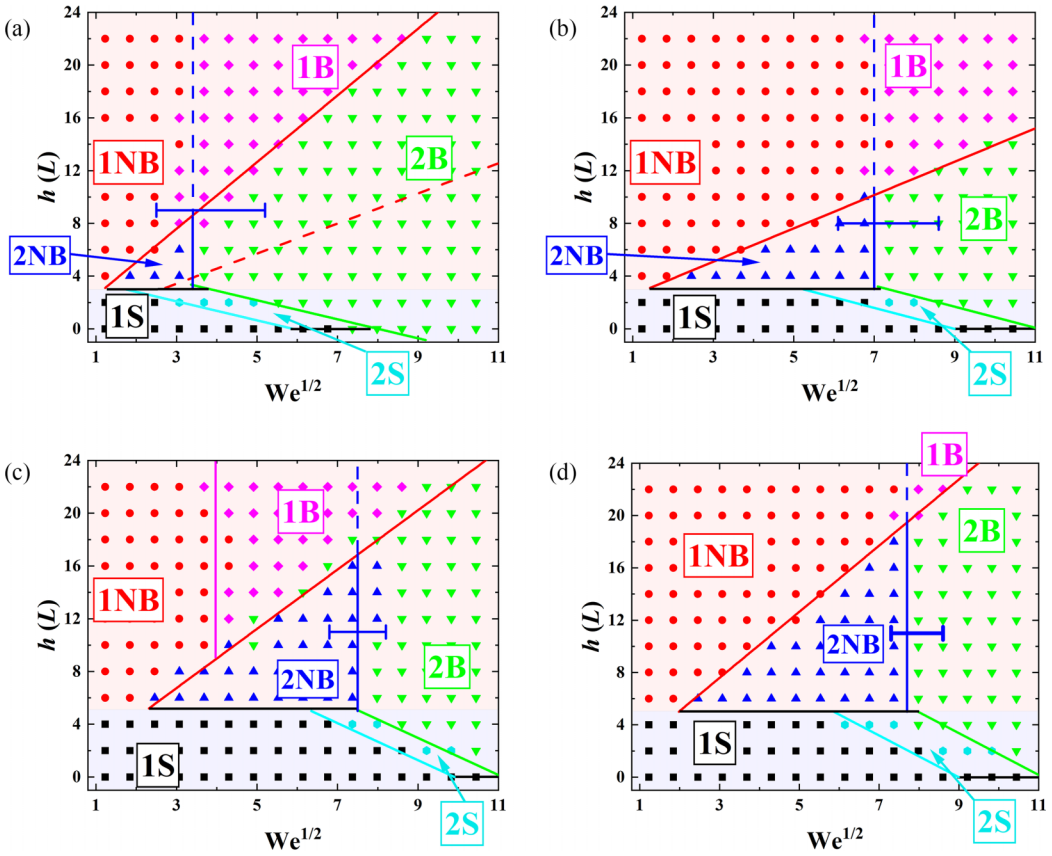

FIG. 6. Phase diagrams of nanodroplets with Oh = 0.35 impacting pillared surfaces with parameter groups of (a) $\varphi = 44\%$, $\theta = 125^\circ$, and $w = 8L$ (series 3), (b) $\varphi = 44\%$, $\theta = 105^\circ$, and $w = 4L$ (series 4), (c) $\varphi = 25\%$, $\theta = 105^\circ$, and $w = 4L$ (series 5), and (d) $\varphi = 44\%$, $\theta = 105^\circ$, $w = 8L$, and $P = 1$ atm (series 6), in which the bouncing nanodroplets on surfaces with $h = 0$ are also classified into the 2B regimes for convenience. Here, the blue solid line stands for the real bouncing boundary on Cassie surfaces. The red dashed line, the green and cyan solid lines, and the blue bar are the predicted results of Eqs. (6), (11), and (14) and Eq. (12), respectively. The red solid line stands for the prediction result of the revised model of the wetting transition, i.e., Eq. (15).

depends on the dynamic contact angle instead of the intrinsic contact angle, and there only exists a small difference between the dynamic contact angles on different hydrophobic pillared surfaces due to the strong inertial force. Certain studies have explored the relationship between the dynamic contact angle and the velocity at contact lines at the nanoscale [51,52]. All of these studies found that a contact line velocity of about $10\,\mathrm{m\,s^{-1}}$ at the nanoscale can lead to an upper dynamic contact angle of 180° on surfaces with intrinsic contact angles from 20° to 140°. In most impact cases in this work, the velocity at the contact line in pillar gaps is much larger than $10\,\mathrm{m\,s^{-1}}$ so the dynamic contact angle almost maintains an extreme value at 180°. Due to the stably large dynamic contact angle, both the intrinsic and dynamic contact angles possibly do not significantly affect the liquid intrusion depth and also the intrusion shape. Therefore, the previous scaling law of $\mathrm{We}_{\mathrm{cri,C\text{-}W}}^{1/2} \sim \varphi h/w(-\cos\theta)$ on Cassie surfaces should be revised to

$$\mathrm{We}_{\mathrm{cri,C\text{-}W}}^{1/2} \sim \varphi h/w. \tag{15}$$

As expected, the revised scaling law with a new prefactor of 7.12 is able to predict all the wetting transition boundaries shown in Fig. 5 and Figs. 6(a)–6(d).

The second failure is the prediction of the bouncing boundary on Cassie surfaces at a low ϕ of 25%, as shown in Fig. 6(c). The bouncing boundaries between 1NB and 1B regimes and between 2NB and 2B regimes are characterized by the same critical Weber number when ϕ is fixed as a relatively high value of 44%, as shown in Fig. 5 and Figs. 6(a) and 6(b) so that the model is able to predict both of them accurately. However, when ϕ is reduced to 25%, these bouncing boundaries no longer have the same critical Weber number, and as a result, the model can only hold for the 2NB-2B boundary but not for the 1NB-1B boundary with the latter having a lower critical Weber number, as shown in Fig. 6(c). For 1NB-1B, the key energy needed to be overcome is the adhesion between the liquid and the top surface of the pillars. When ϕ becomes smaller, the adhesion is decreased so that the required energy is accordingly reduced. Therefore, the decreased critical Weber number can be explained by the weaker adhesion due to the reduced ϕ. Only this situation is out of the prediction of our models. Compared with the predicted 1NB-1B boundary by Eq. (12), the actual boundary shifts towards lower Weber numbers in phase diagrams.

Comparing Fig. 6(d) with Fig. 5, the effect of ambient gas can be discussed. It should be noted that the We range from 1.51 to 109.03 corresponds to the V_0 range from 100 to 850 m s^{-1}, i.e., Mach number (Ma $= V_0/U_s$) can range from 0.29 to 2.5, where $U_s(\approx 340\,\mathrm{m\,s^{-1}})$ is the speed of sound. From the traditional concept, a significant compressibility effect will take place and the motion of impacting nanodroplets will be strongly affected, altering the corresponding phase diagram of outcomes. However, intriguingly, the phase diagram is almost not affected by the filled gas because Fig. 6(d) is nearly the same as Fig. 5; furthermore, the maximum spreading diameter at $P = 0$ and 1 atm also shows as identical, as shown in Fig. S2 of the Supplemental Material [46], violating the expected violent effect of ambient gas. This may be ascribed to the competition of compressibility and rarefaction effects. Indeed, increasing the Mach number usually enhances the compressibility effect, which is a key issue for supersonic flight; however, as the ratio of the mean free path of surrounding gas molecules (λ) to the characteristic length (the droplet diameter D_0 here), i.e., the Knudsen number (Kn $= \lambda/D_0$), becomes large enough, the rarefaction effect also becomes important, which can counteract the mentioned compressibility effect. Zarin [53] quantitively noted that, using the particle Reynolds number ($\mathrm{Re_p} = \rho_g D_0 V_0/\mu_g$), the rarefaction-dominant and compressibility-dominant regimes can be distinguished, where ρ_g and μ_g are the density and viscosity of the surrounding gas. For $\mathrm{Re_p} < 45$, the particle falls in the rarefaction-dominant regime, whereas for $\mathrm{Re_p} > 45$, it transitions from the rarefaction-dominant to the compressibility-dominant regime. Loth [54] proves that in the rarefaction-dominant regime the incompressible theory still holds. Considering nanodroplets falling in an environment filled with nitrogen gas (N_2), i.e., $\rho_g = 6.735\,\mathrm{kg\,m^{-3}}$ and $\mu_g = 17.8\,10^{-6}\,\mathrm{Pa\,s}$, the particle Reynolds number is far below 45, implying that impacting nanodroplets are in the rarefaction-dominant regime so that a violent compressibility effect will not take place during impact. In other words, the impact is more affected by Kn instead of Ma. The mean free path can be calculated by $\lambda = k_B T/(2^{1/2}\pi d^2 P)$, where k_B is the Boltzmann constant, and d is the effective diameter of molecules. Using $T = 300$ K, $d = 0.375$ nm for N_2 [55], and $P = 1$ atm, λ is obtained as 66.3 nm, leading to Kn $= 6.63$. At such a value of Kn, the gas should not be treated as continuous fluid but is reasonable to be regarded as molecular motion. Because less than one hundred N_2 molecules can collide with nanodroplets during the whole impact owing to the extremely small scale of nanodroplets, the gas does not show a significant effect on the impact of nanodroplets. This is a preliminary test, and with further increasing P (i.e., strengthening the collision between nanodroplet and around gas) or using other gas molecules who have larger molecular mass, the significant effect by ambient gas on the impact dynamics may take place. Nonetheless, to a great extent, such a test proves that it is safe to ignore the gas effect on the impact dynamics in N_2 environment (also in air) at a normal gas pressure (1 atm) at the nanoscale.

Besides the issue of the compressibility effect, it is also important to further discuss the viscous effect since the Ohnesorge number for impacting droplets in this work is not altered. The criterion

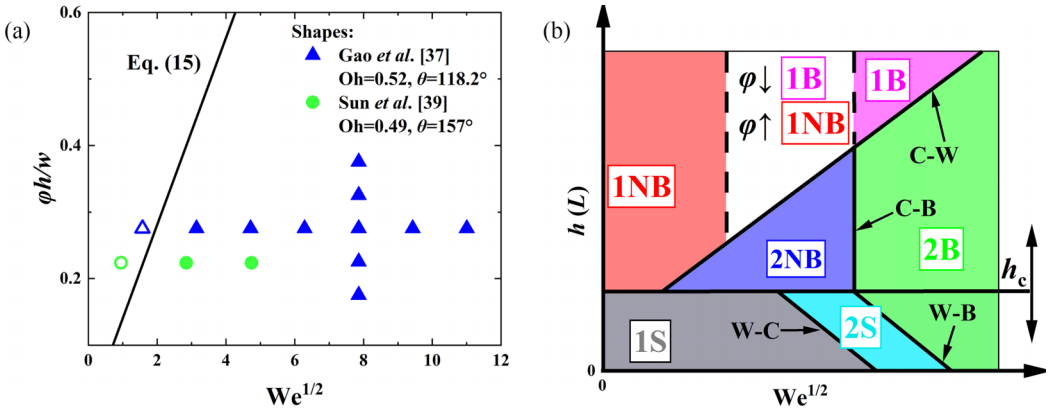

FIG. 7. (a) The comparison between the proposed model of the wetting transition and the data from previous studies with various Oh, where the solid symbols stand for cases of wetting transition and the open ones represent the cases of no wetting transition. (b) Universal phase diagram with all possible outcome regimes and corresponding outcome boundaries determined by the established model of Eq. (16).

of the wetting transition is one of the most concerned criteria due to its effectiveness in measuring the liquid repellency of textured surfaces, and thereby, it is chosen for testing the viscous effect. In the previous study by Lv *et al.* [39], it has been proved that Oh does not affect the criterion of the wetting transition in Oh from 0.247 to 0.452. For further validating whether this transition is truly not sensitive to the viscosity of nanodroplets, the data for different liquid viscosity by TIP4P water (Oh = 0.52) [38] and argon (Oh = 0.49) [40] are drawn in Fig. 7(a) for comparison. As anticipated, the proposed scaling law, i.e., Eq. (15), can successfully predict the boundary for whether impacting nanodroplets experience the wetting transition or not, indicating the wetting transition for nanodroplets is Oh independent in a considerable Oh range of Oh < 0.52. This Oh-independent motion during liquid intrusion in pillar gaps can be attributed to the fact that the slip effect of liquid at the nanoscale is important and even a free-slip condition is partly acceptable [26,56], which can significantly reduce the shear rate and also viscous dissipation in pillar gaps. As a result, the scaling laws for the boundaries of outcomes are expected to be universal for nanodroplets.

Eventually, the scaling laws can be summarized without any adjustable parameters, expressed as

$$\begin{aligned}
\mathrm{We}_{\mathrm{cri,C\text{-}W}}^{1/2} &= c_1\varphi h/w(-\cos\theta),\\
\left[\mathrm{We}_{\mathrm{cri,C\text{-}B}}^{1/2} - (172+188\cos\theta)^{1/2}\right] &= c_2\varphi\cos\theta h_c/w,\\
\left[\mathrm{We}_{\mathrm{cri,W\text{-}C}}^{1/2} + 4.8\varphi - (172+188\cos\theta)^{1/2}\right] &= c_2\varphi\cos\theta h/w,\\
\left[\mathrm{We}_{\mathrm{cri,W\text{-}B}}^{1/2} - (172+188\cos\theta)^{1/2}\right] &= c_2\varphi\cos\theta h/w,
\end{aligned} \tag{16}$$

where $c_1 = 7.12$ and $c_2 = 44$. Based on the proposed model, a universal phase diagram for nanodroplets could be constructed, as shown in Fig. 7(b). On Wenzel surfaces, the 1S, 2S, and 2B regimes are present, and on Cassie surfaces, the 1NB, 2NB, 1B, and 2B exist. Four outcome boundaries, including the 1S-2S boundary (i.e., the dewetting transition boundary on Wenzel surfaces), the 2S-2B boundary (i.e., the bouncing boundary on Wenzel surfaces), the wetting transition boundary on Cassie surfaces, and the bouncing boundary on Cassie surfaces, can be predicted by the established model. The only indeterminate is that, when ϕ is high, the 1NB-1B regimes and the 2NB-2B regimes share the same boundary, whereas the boundary for the 1NB-1B regimes shifts left with a reduced critical Weber number when ϕ is low.

IV. THE MAXIMUM SPREADING FACTOR

A. Effect of liquid intrusion

In addition to constructing phase diagrams to identify outcome regimes, massive efforts have been devoted to modeling the maximum spreading factor, because not only is β_{max} itself is a crucial parameter to evaluate the degree of spreading of impacting droplets on a solid surface, but also modeling it can reveal the underlying energy conversion mechanism during impacts. In Sec. III, liquid intrusion, especially the possible wetting transition between Cassie and Wenzel states, has been attested to play an important role in the outcome regimes of impacting nanodroplets. By modeling β_{max}, the altered spreading dynamics caused by liquid intrusion is desired to be understood. Two kinds of methods have been proposed to predict β_{max}. One is to establish β_{max} from the energy conservation equation; the other is to explore the scaling law of β_{max} based on theoretical analysis or experiment data. However, the former is almost impossible to adopt here due to the significant liquid intrusion effect at the nanoscale. That is, the flow feature in pillar gaps is difficult to generalize because it not only depends on the surface parameters but also relates to whether the wetting transition takes place. Moreover, the irregular shape of the intruding liquid in pillar gaps also makes expressing the surface energy at the maximum spreading state and the viscous dissipation during spreading almost impossible. Therefore, finding the scaling law of β_{max} is preferred.

The data of β_{max} are extracted from our MD simulations under various impact conditions to attempt to find the scaling law of β_{max}. However, the data show that β_{max} depends on We, Oh, θ, and the topology of pillared surfaces (w, h, and ϕ). Therefore, constructing a complete scaling law of β_{max}, relating all of these parameters, is a delicate task. Recently, the scaling laws of β_{max} for impacting nanodroplets on flat surfaces were proposed by Wang *et al.* [22]: $\beta_{max} \sim \mathrm{We}^{1/5}$ at low We (the capillary regime) or $\beta_{max} \sim \mathrm{We}^{1/2}\,\mathrm{Oh}^{1/3}$ at high We (the crossover regime), with the transition between these scaling laws being determined by an impact number, $Q(=\mathrm{We}^{3/10}\,\mathrm{Oh}^{1/3}) = 2.1$. The scaling laws of Wang *et al.* [22] show good agreement with not only their simulation data but also the data from previous studies [23,27,34]. Therefore, the resolution of the delicate task would be readily achieved if a bridge could be established to relate the scaling laws of β_{max} on pillared surfaces to the ones on flat surfaces.

To build this bridge, the following analysis is implemented. The maximum spreading factor characterizes the degree of spreading of impacting droplets. When nanodroplets impact pillared surfaces with the volume of pillar gaps comparable to their volume, the violent liquid intrusion effect can cause a significant reduction in the volume of the bulk droplet (the droplet atop the pillars). Within this context, β_{max} only evaluates the degree of spreading of the bulk droplet. If this assumption is valid, it can be speculated that β_{max} on pillared surfaces should be lower than the one on flat surfaces under the same impact condition, and this speculation has been proven by the present MD simulations. On the other hand, the MD simulations show that the intrusion volume (V_{intr}) at the maximum spreading state is sensitive to the topology of pillared surfaces (w, h, and ϕ), and so is the volume of the bulk droplet ($V_{bulk} = V - V_{intr}$). Here, V is the volume of the entire nanodroplet. Extracting data of β_{max} from the surfaces of different series in this work shows that β_{max} is also significantly dependent on all the topological parameters. Based on these clues above, β_{max} on pillared surfaces is expected to have certain relationships with the one on flat surfaces if the volume of the droplet on flat surfaces is equal to the volume of the bulk droplet. The maximum spreading factors and the volume of the bulk droplet in series 1 ($\theta = 105^\circ$, $w = 8L$, $\varphi = 44\%$) with $h = 22L$ as well as We = 6.0, 18.5, and 63.8 are directly extracted from MD simulations. At the same time, β_{max} is also calculated by the scaling laws on flat surfaces with the extracted V_{bulk}/V, as shown in Fig. 8, where V_{bulk}/V is extracted by the ratio of the number of the molecules within pillar gaps and the total number of molecules for nanodroplets. Astonishingly, the comparison of the extracted β_{max} with the predicted β_{max} shows that they are almost the same, with the maximum relative deviation less than 5%. Inspired by this result, the dominant parameter group can be rewritten as We, Oh, θ, and V_{bulk}/V. This indicates an effective analogy that only the kinetic energy of the bulk droplet

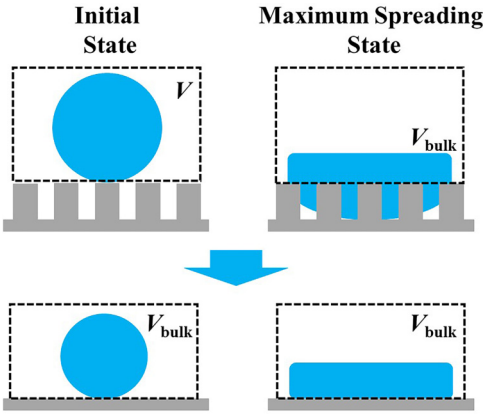

FIG. 8. The schematic of an analogy between impacting nanodroplets on pillared and flat surfaces.

can effectively contribute to the spreading of droplets. Therefore, the kinetic energy for spreading of nanodroplets impacting pillared surfaces is only $(V_{\text{bulk}}/V)E_{\text{k,i}}$. Based on this analogy, replacing the original initial kinetic energy, $E_{\text{k,i}}$, in the scaling laws of Wang *et al.* [22] by $(V_{\text{bulk}}/V)E_{\text{k,i}}$, new scaling laws of $\beta_{\max}$ for nanodroplets impacting pillared surfaces can be obtained.

In a low-We range, Wang *et al.* [22] reported that the impact dynamics of nanodroplets follows the Hertz shock theory. With the liquid intrusion effect, the initial kinetic energy is revised as $(V_{\text{bulk}}/V)E_{\text{k,i}}$; accordingly, the decreased height of an impacting nanodroplet from the initial to maximum spreading states can be obtained from the theory of Hertz shock as [57]

$$\Delta H = D_0\left[\frac{\rho^2 V_0^4}{E^2}(V_{\text{bulk}}/V)^2\right]^{1/5}. \tag{17}$$

Here, Young's modulus can be equivalent to $E = \gamma/(D_0/2)$ [37], and then Eq. (17) can be rearranged as

$$\Delta H = \frac{D_0}{2}[\text{We}(V_{\text{bulk}}/V)]^{2/5}. \tag{18}$$

Using the relationship between the decreased height (ΔH) and the maximum spreading factor $(\beta_{\max})$ on flat surfaces, i.e., $\beta_{\max}^2 \sim \Delta H/D_0$ [57], the scaling law of an impacting nanodroplet on pillared surfaces in a low-We range can be obtained as

$$\beta_{\max} \sim [\text{We}(V_{\text{bulk}}/V)]^{1/5} \Rightarrow \beta_{\max}/(V_{\text{bulk}}/V)^{1/5} \sim \text{We}^{1/5}. \tag{19}$$

Similarly, in a high-We range, Wang *et al.* [22] proposed another scaling law as $\beta_{\max} \sim \text{We}^{1/2}\,\text{Oh}^{1/3}$, representing the energy conversion relation as

$$\text{Oh}^{2/3}\rho D_0^3 V_0^2 \sim \gamma D_{\max}^2. \tag{20}$$

Replacing the initial kinetic energy by $(V_{\text{bulk}}/V)E_{\text{k,i}}$, Eq. (20) is transformed to

$$(V_{\text{bulk}}/V)\text{Oh}^{2/3}\rho D_0^3 V_0^2 \sim \gamma D_{\max}^2. \tag{21}$$

Rearranging Eq. (21) leads to the scaling law for impacting nanodroplets on pillared surfaces in a high-We range as

$$\beta_{\max} \sim [(V_{\text{bulk}}/V)\text{We}]^{1/2}\text{Oh}^{1/3} \Rightarrow \beta_{\max}/(V_{\text{bulk}}/V)^{1/2} \sim \text{We}^{1/2}\text{Oh}^{1/3}. \tag{22}$$

To validate these new scaling laws on pillared surfaces, the values of V_{bulk} are extracted from current MD simulations. As shown in Fig. 9, these two scaling laws agree with the present MD data

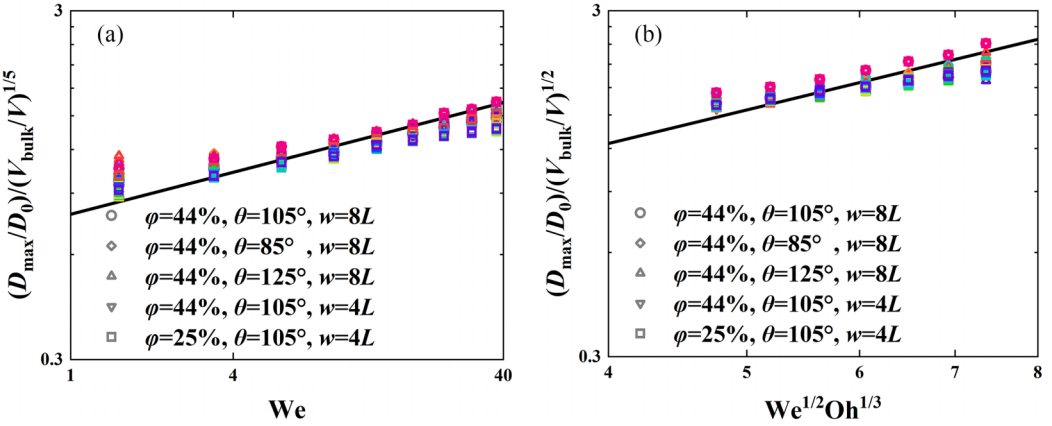

FIG. 9. Comparisons between the proposed scaling laws of β_{max}, Eqs. (19) and (22), and MD data in (a) low- and (b) high-We ranges. The colors changing from red to purple represent h varying from $0L$ to $22L$ with an interval of $2L$. The data of V_{bulk}/V used here are all extracted from MD simulations.

in series 1–5 with a total of 960 data points, by prefactors of Eqs. (19) and (22) being 0.78 and 0.31, respectively, which are almost the same as the ones on flat surfaces [22].

B. Intrusion volume of liquid

The scaling laws of Eqs. (19) and (22) applied to predict β_{max} leave a key problem of how to obtain V_{bulk} instead of extracting it from simulations, i.e., how to quantitatively describe the consumed initial kinetic energy by liquid intrusion during spreading. To solve this issue, the concerned volume of the liquid intruding into pillar gaps ($V-V_{bulk}$) is modeled in this section. Nonetheless, modeling this is extremely challenging work because it not only relates to the multiple dominant parameters but also alters if the wetting transition takes place. Especially, for precisely calculating it, the intrusion morphology is needed. However, previous studies by experiments are difficult to provide detailed information on intrusion morphology owing to the small scale of surface textures. Fortunately, MD simulations can provide not only evidence of the wetting transition but also the opportunity to directly observe the detailed intrusion process. Nonetheless, despite the progress in the impact dynamics on pillared surfaces by MD simulations in recent years, the morphology of liquid intrusion and its dependence on the wetting transition has not been revealed. In this section, the shape of the intrusion front will be classified, and based on the information on intrusion morphology, the intrusion volume ($V-V_{bulk}$) will be modeled.

Figure 10(a) shows the normalized intrusion volume of liquid, i.e., $(V-V_{bulk})/V = 1-V_{bulk}/V$, for all the cases in series 1 (fixed θ, w, and ϕ, and varied h). Two distinct tendencies are observed: (1) a scaling of $1-V_{bulk}/V \sim We^{3/4}$ at relatively high h but low We and(2) another scaling of $1-V_{bulk}/V \sim We^{1/4}$ at relatively low h but high We. Based on the snapshots shown in Fig. 10(b), these two significant tendencies are found to be distinguished by the specific shapes of the intrusion front. In the first intrusion regime, the intrusion front in most cases does not touch the basal wall, leading to an ellipsoidal intrusion front. In the second intrusion regime, the wetting transition does occur so that a Wenzel droplet with the circular-truncated-cone intrusion front is formed. Using different shape assumptions in these intrusion regimes, i.e., an ellipsoidal-front assumption for the first intrusion regime and a circular-truncated-cone-front assumption for the second intrusion regime, the expressions of intrusion volume are expected to be established.

Based on the ellipsoidal-front assumption, the scaling of $1-V_{bulk}/V$ in the first intrusion regime is obtained as

$$1 - V_{bulk}/V \sim D_i^2 h_i / D_0^3, \tag{23}$$

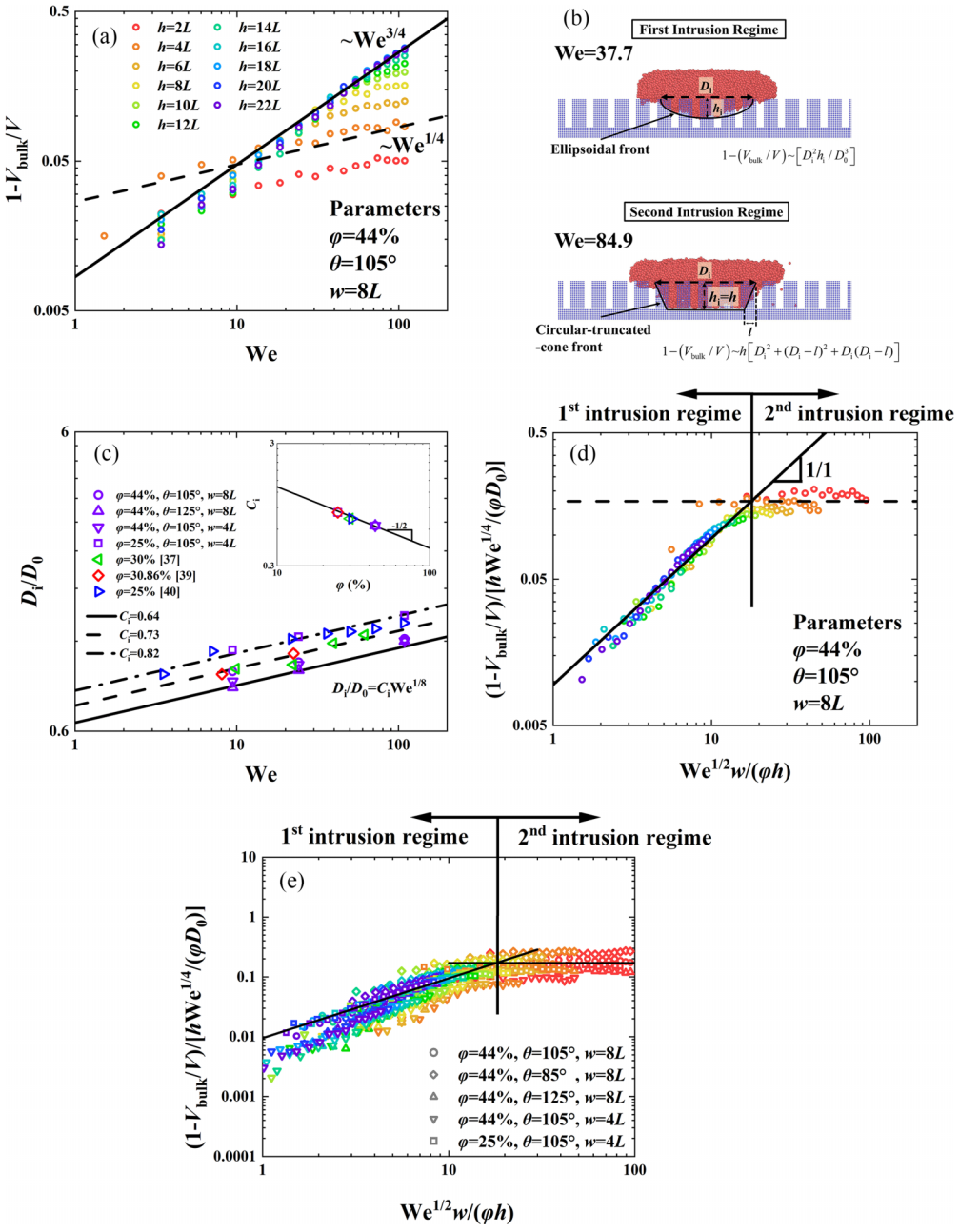

FIG. 10. (a) Normalized intrusion volume of liquid $(1-V_{\text{bulk}}/V)$ for the cases in series 1 varying with We; (b) the schematics for impacting nanodroplets in the first and second intrusion regimes; (c) normalized intrusion diameter (D_i/D_0) varying with We for the current data at $h = 22\ L$ and for the data in the previous study of Gao *et al.* [38] at $\varphi \approx 30\%$, Sun *et al.* [40] at $\varphi = 30.86\%$, and Li *et al.* [41] at $\varphi \approx 25\%$; [(d), (e)] different normalized forms of intrusion volume of liquid varying with Q_i, where the colors changing from red to purple represent h varying from $2L$ to $22L$ with an interval of $2L$, which are the same as the rainbow color legend shown in Fig. 10(a).

where h_i and D_i are the intrusion depth and the intrusion diameter when the volume of the bulk droplet reaches minimal, respectively, as shown in Fig. 10(b). For the intrusion diameter, Lv *et al.* [39] proposed a scaling as $D_i/D_0 \sim \mathrm{We}^{1/4}$; however, this scaling does not agree with the present MD results, as shown in Fig. 10(c). The intrusion diameter is indeed found to rely on We; however, the dependence of D_i/D_0 on We is weaker than the one assumed by Lv *et al.*[39], with a scaling of $D_i/D_0 \sim \mathrm{We}^{1/8}$. Besides, D_i/D_0 almost does not depend on w and θ but it is reduced when ϕ is large. This is attributable to the fact that large ϕ can hinder the intrusion of liquid. Since ϕ represents the ratio of area whereas D_i/D_0 is a dimensionless number of lengths, D_i/D_0 is expected to negatively correlate with $\varphi^{1/2}$, which is proven in Fig. 10(c). As a result, D_i/D_0 scales as $\mathrm{We}^{1/8}/\varphi^{1/2}$. Substituting $h_i \sim w\mathrm{We}^{1/2}/\varphi$ and $D_i/D_0 \sim \mathrm{We}^{1/8}/\varphi^{1/2}$ into Eq. (23), the scaling of $1-V_{\mathrm{bulk}}/V \sim w\mathrm{We}^{3/4}/(\varphi^2 D_0)$ is obtained, which shows the same tendency as the scaling of $1-V_{\mathrm{bulk}}/V \sim \mathrm{We}^{3/4}$ in Fig. 10(a).

In the second intrusion regime, the wetting transition has been completed so that h_i no longer varies with We but always equals h. In such circumstances, there is a circular-truncated-cone intrusion front and the normalized volume of intruding liquid is obtained by

$$1 - V_{\mathrm{bulk}}/V \sim h[{D_i}^2 + (D_i - l)^2 + D_i(D_i - l)]/D_0^3, \tag{24}$$

where l is the difference between the diameters of the circular truncated cone at the upper and lower ends. The relationship of $l \ll D_i$ proved by the snapshots shown in Fig. 10(b) allows Eq. (24) to be simplified as $1-V_{\mathrm{bulk}}/V \sim hD_i^2/D_0^3$. Using $D_i/D_0 \sim \mathrm{We}^{1/8}/\varphi^{1/2}$, the scaling in this intrusion regime is obtained as $1-V_{\mathrm{bulk}}/V \sim h\mathrm{We}^{1/4}/(\varphi D_0)$, which meets the scaling of $1-V_{\mathrm{bulk}}/V \sim \mathrm{We}^{1/4}$ shown in Fig. 10(a).

The scalings in the first and second intrusion regimes are preliminarily obtained as $1-V_{\mathrm{bulk}}/V \sim w\mathrm{We}^{3/4}/(\varphi^2 D_0)$ and $1-V_{\mathrm{bulk}}/V \sim h\mathrm{We}^{1/4}/(\varphi D_0)$, respectively. At the critical transition state, the intrusion volume can be predicted by both these scalings, and thereby the transition criterion between these two regimes can be easily achieved by equating these two scalings, i.e.,

$$w\mathrm{We}_{\mathrm{cri,i}}^{3/4}/(\varphi^2 D_0) \sim h\mathrm{We}_{\mathrm{cri,i}}^{1/4}/(\varphi D_0) \Rightarrow \frac{\mathrm{We}_{\mathrm{cri,i}}^{1/2} w}{\varphi h} = b, \tag{25}$$

where b is a constant. Intriguingly, Eq. (25) has the same form as Eq. (15), proving the assumption that the intrusion mechanisms in the first and second regimes strongly depend on whether the wetting transition takes place. For convenience, an intrusion number for the transition from the first to second intrusion regime is proposed as $Q_i = \mathrm{We}^{1/2}\, w/(\varphi h)$. Replacing the horizontal axis as Q_i and rescaling the vertical axis by the scaling in the second intrusion regime, expressed as $(1-V_{\mathrm{bulk}}/V)/[h\mathrm{We}^{1/4}/(\varphi D_0)]$, a normalized coordinate system is proposed, as shown in Fig. 10(d). Using this coordinate system, the slope of data should be one when $Q_i < b$, indicating the scaling of $1-V_{\mathrm{bulk}}/V \sim w\mathrm{We}^{3/4}/(\varphi^2 D_0)$, whereas such a slope transits from one to zero as $Q_i > b$, showing the scaling of $1-V_{\mathrm{bulk}}/V \sim h\mathrm{We}^{1/4}/(\varphi D_0)$. Therefore, b can be easily by observing the slope change of data in this normalized coordinate. As anticipated, the data in Fig. 10(a) are all collapsed together, as shown in Fig. 10(d), and b is obtained as 18.2. The prefactors of the scalings in the first and second intrusion regimes are 0.17 and 0.0095, respectively. Besides the data of $(1-V_{\mathrm{bulk}}/V)$ in series 1, the other data in series 2–4 are also drawn in such a coordinate system, as shown in Fig. 10(e). Despite no complete collapse, a satisfactory agreement is achieved. Eventually, the model of intrusion volume is obtained as

$$1 - V_{\mathrm{bulk}}/V = \begin{cases} 0.17w\mathrm{We}^{3/4}/(\varphi^2 D_0), & \text{if } Q_i < 18.2 \\ 0.0095h\mathrm{We}^{1/4}/(\varphi D_0), & \text{if } Q_i > 18.2. \end{cases} \tag{26}$$

It should be noted that it does not include additional fitting parameters when incorporating other series data of intrusion volume and it also does not have any adjustable parameters. Besides, since the intrusion volume strongly depends on the wetting transition, the dominant parameters for intrusion volume should be the same as the criterion of the wetting transition. Here, the model of intrusion volume includes We, w, h, ϕ, and D_0 and therefore covers We, w, h, and ϕ, which

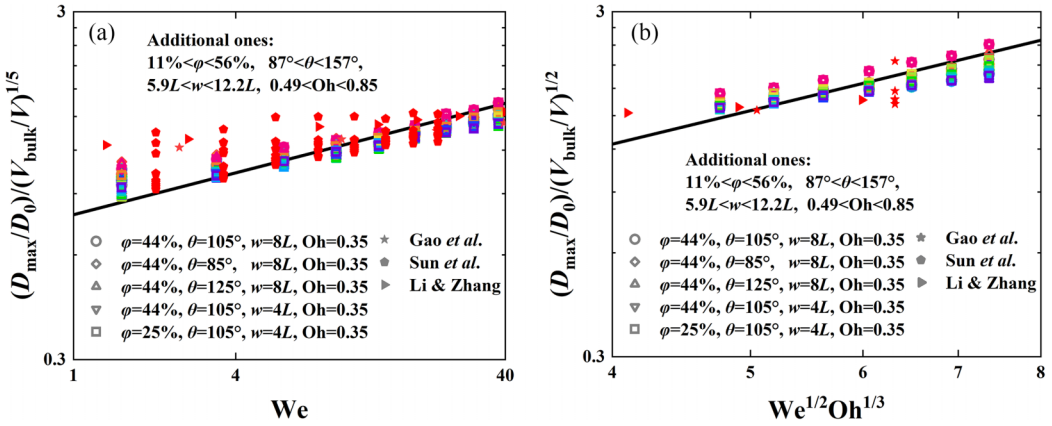

FIG. 11. Comparisons of the MD data extracted from both the present and previous studies with the proposed model, Eqs. (19), (22), and (26), showing good agreement between them in both (a) low- and (b) high-We ranges. The open symbols represent the data in the present work and their colors changing from red to purple represent h varying from $0L$ to $22L$ with an interval of $2L$, which are the same as the rainbow color legend shown in Fig. 9. The red solid symbols stand for the data in the previous studies on pillared surfaces with fixed $h = 18.1$ [38], 14.5 [40], and 17.5 Å [41], respectively, covering other parametric ranges $11\% < \varphi < 56\%$, $87^\circ < \theta < 157^\circ$, $5.9L < w < 12.2L$, and $0.49 < \mathrm{Oh} < 0.85$.

are incorporated in the criterion of the wetting transition. Therefore, Eq. (26) covers all dominant parameters and is reasonable to be universal for nanodroplets. If holding the texture parameters at the nanoscale but altering the droplet diameter to be millimeter sized, Eq. (26) gives $(1-V_{\mathrm{bulk}}/V) \to 0$, which agrees with the previous studies that ignored the intrusion effect of micro- and nanoscale textures during the impact of millimeter-sized droplets [8–10,37].

As a result, substituting Eq. (26) in Eqs. (19) and (22) leads to a complete model of β_{max}. First, β_{max} are predicted by the model for a total of 960 cases in series 1–5 and compared with β_{max} extracted from MD simulations. As shown in Figs. 11(a) and 11(b), the model predictions show good agreement with the present MD simulations, with a mean relative deviation of 6.01%. Second, the data of β_{max} in the previous MD studies [38,40,41] are also used to compare with the model predictions, and good agreement is achieved, as shown in Figs. 11(a) and 11(b). The validation above not only proves the universality of the proposed model but also indicates that the model can hold in extremely wide parametric ranges: $0.22 \leqslant \mathrm{We} \leqslant 109.0$, $0.350 \leqslant \mathrm{Oh} \leqslant 0.846$, $85^\circ \leqslant \theta \leqslant 157^\circ$, $7.88 \leqslant w \leqslant 27.11$ Å, $3.942 \leqslant h \leqslant 43.36$ Å, and $0.11 \leqslant \varphi \leqslant 0.56$, and for at least four kinds of liquids (mW, SPC/E water, TIP4P water, and Ar).

V. CONCLUSIONS

This study comprehensively discusses impact processes of nanodroplets on pillared surfaces, controlled by the parameter group of We, Oh, θ, h, w, and ϕ. Six outcomes are identified, including 1S, 2S, 1NB, 2NB, 1B, and 2B. The 1S, 2S, and 2B regimes can coexist on Wenzel surfaces with the 1S-2S boundary (i.e., the dewetting transition boundary) and the 2S-2B boundary (i.e., the bouncing boundary on Wenzel surfaces) separating them. The 1NB, 2NB, 1B, and 2B regimes take place on Cassie surfaces, which can be distinguished by the wetting transition boundary and the bouncing boundary on Cassie surfaces. The equations of these four boundaries are established, by which a universal phase diagram with six outcome regimes for impacting nanodroplets on pillared surfaces is therefore proposed.

The principal difference between the spreading dynamics on flat and pillared surfaces is ascribed to the significant liquid intrusion effect. With an assumption that only the initial kinetic energy of the bulk droplet contributes to spreading, the effect of the bulk droplet and the liquid intruding into

pillar gaps is successfully decoupled. This assumption is verified by replacing the initial kinetic energy term, $E_{k,i}$, in the scaling laws of the maximum spreading factor (β_{max}) on flat surfaces by $E_{k,i}V_{bulk}/V$, which successfully predicts β_{max} on pillared surfaces.

Here, the normalized intrusion volume ($1-V_{bulk}/V$) is modeled for obtaining the expression of the bulk volume (V_{bulk}). There exist two intrusion regimes with an ellipsoidal intrusion front and a circular-truncated-cone intrusion front. Based on these morphologies, the scalings of intrusion volume are established as $1-V_{bulk}/V \sim w\mathrm{We}^{3/4}/(\varphi^2 D_0)$ in the first intrusion regime and $1-V_{bulk}/V \sim h\mathrm{We}^{1/4}/(\varphi D_0)$ in the second intrusion regime. Subsequently, by equaling these scalings, a criterion for the transition from the first to the second intrusion regime is proposed as $Q_i \equiv \mathrm{We}^{1/2}\, w/(\varphi h) = 18.2$. The model of intrusion volume shows good agreement with all the present MD results of $1-V_{bulk}/V$. Eventually, scaling laws of β_{max} in the capillary and crossover regimes for impacting nanodroplets on pillared surfaces are derived by substituting the model of intrusion volume in the scaling laws on flat surfaces above. The developed scaling laws of β_{max} not only fit well with all the present MD results of β_{max} but also show a strong ability to predict β_{max}, provided that the pillared parameters and the intrinsic contact angle are known.

ACKNOWLEDGMENTS

This study was partially supported by the State Key Program of National Natural Science of China (Grant No. 51936004), Science Fund for Creative Research Groups of the National Natural Science Foundation of China (Grant No. 51821004).

The authors report no conflict of interest.

[1] T. Kawase, T. Shimoda, C. Newsome, H. Sirringhaus, and R. H. Friend, Inkjet printing of polymer thin film transistors, Thin Solid Films **438–439**, 279 (2003).

[2] A. Alizadeh, Dynamics of ice nucleation on water repellent surfaces, Langmuir **28**, 3180 (2012).

[3] G. Liang and I. Mudawar, Review of spray cooling—Part 1: Single-phase and nucleate boiling regimes, and critical heat flux, Int. J. Heat Mass Transfer **115**, 1174 (2017).

[4] X. Deng, F. Schellenberger, P. Papadopoulos, D. Vollmer, and H. J. Butt, Liquid drops impacting superamphiphobic coatings, Langmuir **29**, 7847 (2013).

[5] A. L. Yarin, Drop impact dynamics: Splashing, spreading, receding, bouncing …, Annu. Rev. Fluid Mech. **38**, 159 (2006).

[6] C. Ukiwe and D. Y. Kwok, On the maximum spreading diameter of impacting droplets on well-prepared solid surfaces, Langmuir **21**, 666 (2005).

[7] Z. Wang, C. Lopez, A. Hirsa, and N. Koratkar, Impact dynamics and rebound of water droplets on superhydrophobic carbon nanotube arrays, Appl. Phys. Lett. **91**, 023105 (2007).

[8] C. Antonini, A. Amirfazli, and M. Marengo, Drop impact and wettability: From hydrophilic to superhydrophobic surfaces, Phys. Fluids **24**, 102104 (2012).

[9] J. B. Lee, N. Laan, K. G. de Bruin, G. Skantzaris, N. Shahidzadeh, D. Derome, J. Carmeliet, and D. Bonn, Universal rescaling of drop impact on smooth and rough surfaces, J. Fluid Mech. **786**, R4 (2016).

[10] S. Wildeman, C. W. Visser, C. Sun, and D. Lohse, On the spreading of impacting drops, J. Fluid Mech. **805**, 636 (2016).

[11] T. Srivastava and S. Kondaraju, Analytical model for predicting maximum spread of droplet impinging on solid surfaces, Phys. Fluids **32**, 092103 (2020).

[12] J. Du, X. Wang, Y. Li, Q. Min, and X. Wu, Analytical consideration for the maximum spreading factor of liquid droplet impact on a smooth solid surface, Langmuir **37**, 7582 (2021).

[13] J. Eggers, M. A. Fontelos, C. Josserand, and S. Zaleski, Drop dynamics after impact on a solid wall: Theory and simulations, Phys. Fluids **22**, 062101 (2010).

[14] R. Zhang, S. Farokhirad, T. Lee, and J. Koplik, Multiscale liquid drop impact on wettable and textured surfaces, Phys. Fluids **26**, 082003 (2014).
[15] T. Kondo and K. Ando, Simulation of high-speed droplet impact against a dry/wet rigid wall for understanding the mechanism of liquid jet cleaning, Phys. Fluids **31**, 013303 (2019).
[16] A.-L. Biance, F. Chevy, C. Clanet, G. Lagubeau, and D. Quéré, On the elasticity of an inertial liquid shock, J. Fluid Mech. **554**, 47 (2006).
[17] P. Attané, F. Girard, and V. Morin, An energy balance approach of the dynamics of drop impact on a solid surface, Phys. Fluids **19**, 012101 (2007).
[18] P. Galliker, J. Schneider, H. Eghlidi, S. Kress, V. Sandoghdar, and D. Poulikakos, Direct printing of nanostructures by electrostatic autofocussing of ink nanodroplets, Nat. Commun. **3**, 890 (2012).
[19] M. J. Kreder, J. Alvarenga, P. Kim, and J. Aizenberg, Design of anti-icing surfaces: Smooth, textured or slippery?, Nat. Rev. Mater. **1**, 1 (2016).
[20] M. W. Glasscott, A. D. Pendergast, S. Goines, A. R. Bishop, A. T. Hoang, C. Renault, and J. E. Dick, Electrosynthesis of high-entropy metallic glass nanoparticles for designer, multi-functional electrocatalysis, Nat. Commun. **10**, 2650 (2019).
[21] M. Benz, A. Asperger, M. Hamester, A. Welle, S. Heissler, and P. A. Levkin, A combined high-throughput and high-content platform for unified on-chip synthesis, characterization and biological screening, Nat. Commun. **11**, 5391 (2020).
[22] Y.-F. Wang, Y.-B. Wang, X. He, B.-X. Zhang, Y.-R. Yang, X.-D. Wang, and D.-J. Lee, Scaling laws of the maximum spreading factor for impact of nanodroplets on solid surfaces, J. Fluid Mech. **937**, A12 (2022).
[23] Y. B. Wang, Y. F. Wang, S. R. Gao, Y. R. Yang, X. D. Wang, and M. Chen, Universal model for the maximum spreading factor of impacting Nanodroplets: From hydrophilic to hydrophobic surfaces, Langmuir **36**, 9306 (2020).
[24] Q. Ma, Y.-F. Wang, Y.-B. Wang, X. He, S.-F. Zheng, Y.-R. Yang, X.-D. Wang, and D.-J. Lee, Phase diagram for nanodroplet impact on solid surfaces, Phys. Fluids **33**, 102007 (2021).
[25] F. F. Xie, S. H. Lv, Y. R. Yang, and X. D. Wang, Contact time of a bouncing nanodroplet, J. Phys. Chem. Lett. **11**, 2818 (2020).
[26] Y.-F. Wang, Y.-B. Wang, Z.-H. Cai, Q. Ma, Y.-R. Yang, S.-F. Zheng, D.-J. Lee, and X.-D. Wang, Binary collision dynamics of equal-sized nanodroplets, J. Fluid Mech. **979**, A25 (2024).
[27] X.-H. Li, X.-X. Zhang, and M. Chen, Estimation of viscous dissipation in nanodroplet impact and spreading, Phys. Fluids **27**, 052007 (2015).
[28] J. Koplik, J. R. Banavar, and J. F. Willemsen, Molecular dynamics of poiseuille flow and moving contact lines, Phys. Rev. Lett. **60**, 1282 (1988).
[29] Y.-F. Wang, Y.-B. Wang, C.-L. Zhang, X. He, Y.-R. Yang, S.-F. Zheng, D.-J. Lee, and X.-D. Wang, Retraction and bouncing dynamics of nanodroplets upon impact on superhydrophobic surfaces, Phys. Fluids **35**, 032012 (2023).
[30] Y.-F. Wang, Y.-B. Wang, X. He, B.-X. Zhang, Y.-R. Yang, X.-D. Wang, and D.-J. Lee, Retraction dynamics of low-viscosity nanodroplets: From hydrophobic to hydrophilic surfaces, J. Mol. Liq. **355**, 118963 (2022).
[31] Y.-B. Wang, Y.-F. Wang, Y.-R. Yang, X.-D. Wang, and M. Chen, Spreading time of impacting nanodroplets, J. Phys. Chem. B **125**, 5630 (2021).
[32] Y. B. Wang, Y. F. Wang, X. Wang, B. X. Zhang, Y.-R. Yang, D.-J. Lee, X.-D. Wang, and M. Chen, Splash of impacting nanodroplets on solid surfaces, Phys. Rev. Fluids **6**, 094201 (2021).
[33] Y. B. Wang, X. D. Wang, Y. R. Yang, and M. Chen, The maximum spreading factor for polymer nanodroplets impacting a hydrophobic solid surface, J. Phys. Chem. C **123**, 12841 (2019).
[34] B. X. Li, X. H. Li, and M. Chen, Spreading and breakup of nanodroplet impinging on surface, Phys. Fluids **29**, 012003 (2017).
[35] C. Clanet, C. Beguin, D. Richard, and D. Quéré, Maximal deformation of an impacting drop, J. Fluid Mech. **517**, 199 (2004).
[36] W. Barthlott and C. Neinhuis, Purity of the sacred lotus, or escape from contamination in biological surfaces, Planta **202**, 1 (1997).
[37] D. Richard, C. Clanet, and D. Quéré, Contact time of a bouncing drop, Nature (London) **417**, 811 (2002).

[38] S. Gao, Q. Liao, W. Liu, and Z. Liu, Nanodroplets impact on rough surfaces: A simulation and theoretical study, Langmuir **34**, 5910 (2018).
[39] S.-H. Lv, F.-F. Xie, Y.-R. Yang, D.-J. Lee, X.-D. Wang, and Y.-Y. Duan, Impact regimes of nanodroplets impacting nanopillared surfaces, Phys. Rev. Fluids **7**, 034203 (2022).
[40] L. Sun, J. Pan, X. Wang, and D. Jing, Molecular dynamics study of nanoscale droplets impacting on textured substrates of variable wettability, Phys. Fluids **34**, 012005 (2022).
[41] H. Li and K. Zhang, Dynamic behavior of water droplets impacting on the superhydrophobic surface: Both experimental study and molecular dynamics simulation study, Appl. Surf. Sci. **498**, 143793 (2019).
[42] D. Bartolo, F. Bouamrirene, E. Verneuil, A. Buguin, P. Silberzan, and S. Moulinet, Bouncing or sticky droplets: Impalement transitions on superhydrophobic micropatterned surfaces, Europhys. Lett. **74**, 299 (2006).
[43] T. Deng, K. K. Varanasi, M. Hsu, N. Bhate, C. Keimel, J. Stein, and M. Blohm, Nonwetting of impinging droplets on textured surfaces, Appl. Phys. Lett. **94**, 133109 (2009).
[44] V. Molinero and E. B. Moore, Water modeled as an intermediate element between carbon and silicon, J. Phys. Chem. B **113**, 4008 (2009).
[45] X. He, B.-X. Zhang, Y.-F. Wang, Y.-Y. Zhang, Y.-R. Yang, X.-D. Wang, and D.-J. Lee, Dynamic coalescence of two charged droplets with deflected angles in the presence of electric fields, J. Mol. Liq. **353**, 118812 (2022).
[46] See Supplemental Material at http://link.aps.org/supplemental/10.1103/PhysRevFluids.9.073602 for the comparison of the maximum spreading factors between impacting mW nanodroplets and Ar nanodroplets (Fig. S1); the comparison of the maximum spreading factors between impacting mW nanodroplets at gas pressures of 0 and 1 atm (Fig. S2); and the method to calculate the available energy.
[47] N. A. Patankar, Transition between superhydrophobic states on rough surfaces, Langmuir **20**, 7097 (2004).
[48] T. Koishi, K. Yasuoka, S. Fujikawa, T. Ebisuzaki, and X. C. Zeng, Coexistence and transition between Cassie and Wenzel state on pillared hydrophobic surface, Proc. Natl. Acad. Sci. USA **106**, 8435 (2009).
[49] J. N. Israelachvili, *Intermolecular and Surface Forces* (Academic Press, New York, 2011).
[50] X. He, B.-X. Zhang, S.-L. Wang, Y.-F. Wang, Y.-R. Yang, X.-D. Wang, and D.-J. Lee, The Cassie-to-Wenzel wetting transition of water films on textured surfaces with different topologies, Phys. Fluids **33**, 112006 (2021).
[51] D. Seveno, G. Ogonowski, and J. De Coninck, Liquid coating of moving fiber at the nanoscale, Langmuir **20**, 8385 (2004).
[52] E. Bertrand, T. D. Blake, and J. De Coninck, Influence of solid–liquid interactions on dynamic wetting: A molecular dynamics study, J. Phys.: Condens. Matter **21**, 464124 (2009).
[53] N. A. Zarin, Measurement of non-continuum and turbulence effects on subsonic sphere drag, NASA, No. NASA-CR-1585 (1970).
[54] E. Loth, Compressibility and rarefaction effects on drag of a spherical particle, AIAA J. **46**, 2219 (2008).
[55] S. Kunze, R. Groll, B. Besser, and J. Thöming, Molecular diameters of rarefied gases, Sci. Rep. **12**, 2057 (2022).
[56] Y. F. Wang, Y. B. Wang, F. F. Xie, J. Y. Liu, S. L. Wang, Y. R. Yang, S. R. Gao, and X. D. Wang, Spreading and retraction kinetics for impact of nanodroplets on hydrophobic surfaces, Phys. Fluids **32**, 092005 (2020).
[57] L. D. Landau and E. M. Lifshits, *Theory of Elasticity* (Fizmatlit Publishers Russia, Moscow, 1965).